Gray-box modeling and model-based control of Czochralski process producing 300 mm diameter Silicon ingots

Shota Kato

2021

Contents

Chapter 1 General Introduction 1

1.1 Introductory Remark 1

1.2 Czochralski process 2

1.3 Control method of CZ process 4

1.4 Thesis Objectives 7

Chapter 2 Gray-box modeling of the Czochralski process 9

2.1 Introduction 9

2.2 EHG model of CZ process 11

2.2.1 Energy transfer model 12

2.2.2 Hydrodynamic and geometrical model 17

2.2.3 Issue of EHG model 18

2.3 Proposed gray-EHG model 19

2.3.1 Training data for statistical model 19

2.3.2 Statistical model 21

2.3.3 Prediction accuracy of statistical model 22

2.4 Results and Discussion 22

2.4.1 Simulation Conditions 23

2.4.2 Prediction results 23

2.4.3 Discussion 26

2.5 Conculusion 26

Chapter 3 Gray-box model-based predictive control 28

3.1 Introduction 28

3.2 Proposed control method 30

3.2.1 Successive linearization 30

3.2.2 Optimization problem of model predictive control 32

3.3 Simulation condition 32

3.4 Results 34

3.4.1 Linearization of gray-box model 34

3.4.2 Control simulation 36

3.5 Conclusion 37

Chapter 4 Successive model update 40

4.1 Introduction 40

4.2 Proposed method 42

4.3 Simulation condition 44

4.4 Results and Discussion 45

4.5 Conclusion 50

Chapter 5 Conclusion / Future Perspectives 52

5.1 Summary 52

5.2 Future Outlooks 54

References 55

Acknowledgements 63

Chapter 1

General Introduction

1.1 Introductory Remark

Silicon (Si) wafers are raw materials for semiconductors, which are vital components of most electronic goods, including computers, telecommunication products, and consumer electronics. SEMI Silicon Manufacturers' Group (SMG) reported that worldwide Si wafer area shipments in 2020 are 1.3 times larger than that in 2010 and 1.05 times larger than that in 2019 [1]. SMG also reported that the shipments increased 6% to 3,534 million square inches in the second quarter of 2021, surpassing the historical high set in the first quarter, and second quarter 2021 Si wafer shipments grew 12% from the 3,152 million square inches recorded during the same quarter last year [2]. Worldwide Semiconductor Trade Statistics (WSTS) forecasted that the global semiconductor market would grow from 6.8 percent in 2020 to 19.7 percent in 2021. [3]. Demand for semiconductors has been growing due to the increasing demand for personal computers and tablet devices as people spend more time at home. The widespread of 5G smartphones and an increase in capital investment demand for cloud services and other infrastructure also influence the demand for semiconductors. However, a shortage of semiconductors has been an issue, affecting the production of semiconductor-related products such as

motor vehicles. Although investments are being made to enhance manufacturing capacity around the world, it takes at least one year to start running a new production line, and even after the start, the lead time for semiconductor production is said to be three to six months.

Semiconductors are manufactured by forming electronic circuits on Si wafers. Si wafers are produced in only one way: by slicing Si ingots [4]. Manufacturing high-quality ingots with high efficiency is essential to obtain high-quality Si wafers efficiently.

In the field of monosilicon crystal growth, two methods have been well established: the Czochralski (CZ) and the floating zone (FZ) methods. The CZ method has produced more than 95% of monocrystalline Si in the current semiconductor industry, while the FZ method is only used for niche products such as high power devise because the FZ method can produce a lower oxygen content crystal [5–7].

1.2 Czochralski process

The CZ process is a method to produce Si ingots developed by Jan Czochralski and has become the most dominant method for producing monocrystalline Si ingots [4].

A schematic diagram of the CZ process is shown in Fig. 1.1. In the furnace, a quartz crucible is surrounded by a heater and shield. Polycrystalline Si is first charged into the crucible and melted by the heater. Then, a seed of the crystal is attached to the surface of the melt. The crystal starts to grow when the seed is pulled up. Due to the surface tension between the seed and the melt, a meniscus section, which is a thin film of the melt, is formed. The crystal grows at the solid-liquid interface, which is the top of the meniscus section. During the crystal growth, the crucible and the crystal are rotated in opposite directions. The crystal consists of three parts: the neck part, the body of the crystal, and the tail part.

This dissertation focuses on the production of the ingot body, which requires a longer

time than the production of the other parts. During the ingot body production, keeping the crystal radius and growth rate constant is crucial to produce defect-free crystals and reduce the loss in the subsequent process. It is also necessary to control the position of the melt so that the thermal environment around the solid-liquid interface does not change rapidly. In the industrial CZ process, the desired quality of the product is obtained by manipulating three variables: the power input to the heater, the crystal pulling rate, and the crucible rise rate.

The larger size of the Si wafer enables the production of more chips; if the diameter is increased by a factor of 1.5, the surface area is increased by a factor of 2.25. In addition, the larger diameter reduces the dead space around the wafer and the area of fluctuation around the wafer during manufacturing. The fact will further increase the number of chips obtained from one wafer. For these reasons, the diameter of the Si wafer has been increasing along with the progress of manufacturing technology. At the beginning of the 1970s, the diameter was at 50 mm, and this had reached 100 mm in 1980, then 200 mm in 1990, and 300 mm in 1995 [8]. Although the production of 300 mm wafers became possible in 1995, mass production of 300 mm wafers is started in 2001 [9]. The CZ process can produce an ingot up to 450 mm in diameter, which weighs about 800

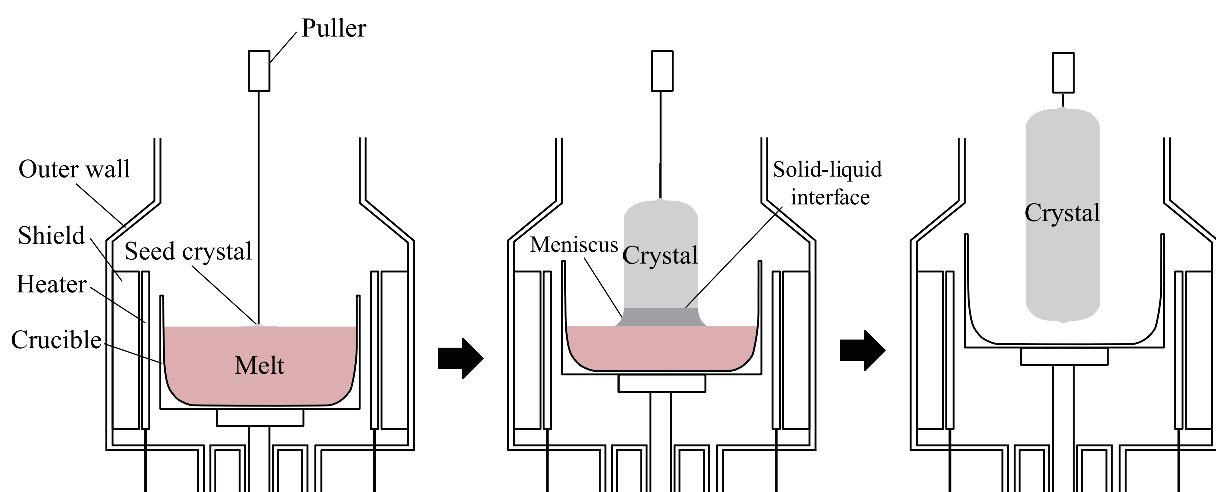

Fig. 1.1: Schematic diagram of the CZ process.

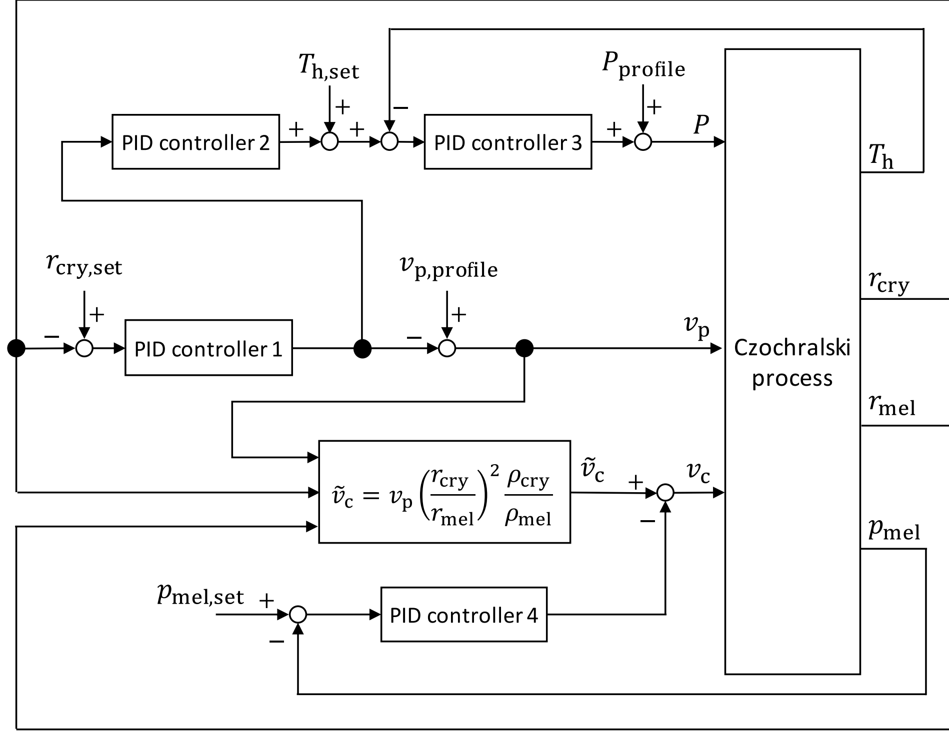

Fig. 1.2: Block flow diagram of the industrial Czochralski process. Manipulated variables are P, v_p, and v_c. Controlled variables are the heater temperature T_h, the crystal radius r_{cry}, and the melt position p_{mel}. Subscripts set and profile denote a set-point and a profile. r_{mel}, ρ_{cry}, and ρ_{mel} denote the radius of the melt surface, the crystal density, and the melt density, respectively.

kg and takes three days to grow [7]. Currently, 200 and 300 mm-diameter crystals have become standard for various devices because they can stably provide a huge amount of high-quality wafers at low cost [10].

1.3 Control method of CZ process

The block flow diagram of the current industrial CZ process is represented in Fig. 1.2, where subscripts set and profile mean a set-point and profile. The crystal radius r_{cry}, the heater temperature T_h, and the melt position p_{mel} are controlled by manipulating the crystal pulling rate v_p, the crucible rise rate v_c, and the heater input power P. p_{mel} is a distance between the melt surface and the bottom of the shield above the melt.

The crystal growth rate v_{g} cannot be measured in real time; thus, v_{p} is manipulated to track the predetermined value $v_{\mathrm{p,profile}}$ in order to control v_{g}. The melt surface radius r_{mel} changes as the crystal grows since the crucible is bowl-shaped. ρ_{cry} and ρ_{mel} are the density of the crystal and melt.

The CZ process is characterized by a long time constant between P and the controlled variables (CVs). Also, the input-output relationship changes over time due to the decrease in melt volume with crystal growth, and the relationship is nonlinear because the radiative heat transfer is dominant in the furnace. When designing a control system of the CZ process, it is also essential to consider that the transfer functions from the manipulated variables (MVs) to the CVs have different time constants. Specifically, changes in v_{p} and v_{c} affect the CVs faster than P. There is a desire to produce higher quality 300 mm Si wafers at a lower cost for the application of the 300 mm Si wafers to power devices [10]. However, the conventional control method based on PID control cannot significantly improve its control performance because of the nonlinear and time-varying characteristics.

Several control methods have been developed to achieve higher control performance. Gevelber et al. proposed a model-based multi-loop control system [11–14]. They investigated the importance of controlling the shape of the interface in addition to r_{cry} in terms of minimizing the number of crystal defects. The model was constructed to reflect the effect of radiation heat transfer in the furnace, and a control structure was developed to realize both r_{cry} and the shape of the interface.

Another approach is developed by Winkler et al. [15, 16]. Their approach is based on the fact that it is easier to derive a sufficiently accurate model of meniscus dynamics than to build a sufficiently accurate thermal behavior model. Using the model of the meniscus dynamics, the model-based controller calculates the desired value of $v_{\mathrm{p}}/v_{\mathrm{g}}$, the ratio of v_{p} to v_{g}. They positioned PID controllers around this model-based controller and manipulated v_{p} and P.

There also exist studies using the control structure of the industrial CZ process. The control performance of the industrial control structure depends on the feedforward trajectories of v_{p} and T_{h}. Lee et al. [17] and Zhang et al. [18] utilized a model to determine a feedforward trajectory of T_{h} in the traditional control structure.

The studies mentioned above are based on the lumped parameter model, while several studies developed distributed parameter models [19–21]. However, it is difficult to use these methods in practice because the MVs in these models are also spatially distributed [22].

Some of the previous studies utilize statistical models. Ren et al. [23] constructed a deep neural network by combining a stacked autoencoder and a long short-term memory (LSTM) network to capture the features and dynamics of the crystal growth. They used the model to design two controllers, which control r_{cry} and T_{h} by manipulating v_{p} and P, respectively. Ren et al. [24] developed a Hammerstein-Wiener model based on an LSTM network for the energy transfer process and combined the model with the hydrodynamic and geometric model. They applied the model to the control of r_{cry} and verified the effectiveness.

Considering the nonlinearity and time delay of the CZ process, model predictive control (MPC) is expected to achieve higher control performance than the conventional PID control. Irizarry-Rivera and Seider [25, 26] developed two model predictive controllers: one controls r_{cry} by manipulating v_{p}, and the other controls v_{p} by manipulating P. Abdollahi et al. [27] derived the optimal temperature trajectory using quadratic programming and then implemented an MPC strategy to track the optimal temperature. Rahmanpour et al. [28, 29] developed a control strategy with two model predictive controllers to control r_{cry} and melt temperature T_{mel}.

Recent several studies on MPC use statistical models. Liu et al. [30] built a stacked sparse autoencoder model with the input as r_{cry} and the output as T_{h}. They then desigend a control structure in which r_{cry} and T_{h} are controlled by manipulating P with

constant v_p. Wan et al. [31] proposed a soft-sensor estimating v_g/G, a ratio of v_g to the axial temperature gradient at the solid-liquid interface G. They also designed a dual closed-loop control strategy to control r_cry and v_g/G. The CZ process is a batch process; thus, the operating conditions are different in each batch. Besides, the heat transfer from the heater varies with time because the melt volume and crystal length vary with time. The data covering these changes need to be prepared to achieve acceptable performance in the statistical model-based MPC. In addition, if the parameters in the statistical models are not set properly or the model is not well-tuned, the predictive performance of the model will deteriorate. In general, there is no fixed rule for tuning these parameters, and in most cases, these parameters are determined by trial and error [30].

1.4 Thesis Objectives

The industrial CZ processes mainly produce Si ingots with a diameter of 300 mm; however, there have been few studies [17, 18] on the process for 300 mm-diameter ingot production. Although Zheng et al. [32] developed a first-principle model to predict r_cry and v_g from P, v_p, and v_c in the process producing 300 mm Si ingots, there have been no model predicting the three variables (r_cry, v_g, and T_h). In the first-principle model, the values of variables that cannot be measured at the start of the prediction are determined by trial-and-error, and thereby, highly accurate predictions can be made only in a limited period.

This dissertation aims to develop an MPC system for the industrial CZ process with higher control performance than the conventional control system. First, a gray-box model is developed by improving the first-principle model proposed by Zheng et al. [32]. Then, a nonlinear MPC method based on the gray-box model is developed. We further develop a method for updating the prediction model to achieve high disturbance

rejection performance even when a large plant-model mismatch exists.

The structure of this dissertation is shown below.

In Chapter 2, we describe the gray-box modeling of the CZ process. First, a review of conventional models and the issues of the models are presented. To solve the issues, we construct a statistical model estimating the variable that highly affects the prediction accuracy of the CVs. We also propose a method for determining unmeasured variables, which is the reason for the limited validation data in the previous study [32]. The prediction accuracy of the proposed gray-box model and the conventional first-principle model is verified using four ingot production data.

The model can predict the CVs with high accuracy, but it consists of high-dimensional complex differential-algebraic equations. Therefore, it is difficult to solve the optimization problem in the nonlinear MPC scheme using the gray-box model. To deal with the challenge, we apply successive linearization proposed by Megías et al. [33] and propose the control method based on the gray-box model in Chapter 3. We compare the disturbance rejection performance of the proposed method with that of the conventional control method used in the industrial CZ process through simulations.

In Chapter 3, we conduct simulations with a plant-model mismatch: one of the parameters in the prediction model is 5 or 10% different from that in the controlled process. In practical applications, there would exist a more significant plant-model mismatch. Hence, in Chapter 4, we propose a method for successively updating the prediction model based on moving horizon estimation. The effectiveness of the model update is verified by comparing the gray-box model-based predictive control methods with and without a model update.

In Chapter 5, the general conclusion — the summarization of this dissertation and the future perspectives — is presented.

Chapter 2

Gray-box modeling of the Czochralski process

2.1 Introduction

Table 2.1 summarizes the models of CZ processes for the control system design in previous studies. Gevelber and Stephanopoulos [34] developed a physical model representing the relationship between P, v_{p}, and r_{cry}. Winkler et al. [15, 16] and Neubert and Winkler [35] derived a physical model representing the relationship between v_{p}, v_{c}, and r_{cry}, by taking into account the mass balance and geometric relationship. Satunkin [36] developed a model based on the mass conservation law, the heat balance, and the thermodynamic equilibrium condition at the three-phase line, with v_{p} and melt temperature T_{mel} as inputs and r_{cry} and meniscus height h_{men} as outputs. Abdollahi and Dubljevic [37] and Abdollahi et al. [27] constructed a physical model to represent the relationship between P, v_{p}, r_{cry}, and T_{mel}, considering the radiative heat transfer from the heater and the conductive heat transfer in the crystal. Rahmanpour et al. [28] developed a simple model with fewer states and parameters than the above models, with P and v_{p} as inputs and r_{cry} and T_{mel} as outputs. All of the above models were built for

Table 2.1: Input and output variables and the target crystal diameter of the models built for the control system design of the CZ process in previous studies. The model type is either physical (P), statistical (S), or gray-box (G).

Reference	Model type	Input variable	Output variable	Crystal diameter [mm]
[34]	P	P, v_{p}	r_{cry}	40
[15, 16, 35]	P	v_{p}, v_{c}	r_{cry}	55
[36]	P	v_{p}, T_{mel}	r_{cry}, h_{men}	80
[37, 38]	P	P, v_{p}	r_{cry}, T_{mel}	100
[28]	P	P, v_{p}	r_{cry}, T_{mel}	160
[17]	S	T_{h}	v_{p}	200, 300
[18]	S	T_{h}	v_{p}	300
[32]	P	P, v_{p}, v_{c}	r_{cry}, v_{g}	300
Present study	G	P, v_{p}, v_{c}	r_{cry}, v_{g}, T_{h}	300

ingot production processes with a diameter of less than 200 mm. Since 300 mm diameter single-crystal silicon ingots are currently mass-produced, a model that can represent the dynamic characteristics of the industrial-scale CZ process is required [10]. Lee et al. [17] and Zhang et al. [18] constructed models whose input and output are T_{h} and v_{p}. Zheng et al. [32] developed a first-principle model to compute r_{cry} and v_{g} from P, v_{p}, and v_{c} for a process to produce 300 mm diameter single-crystal silicon ingots, and showed that the model simulated r_{cry} and v_{g} with high accuracy using real process data.

None of the previous models can accurately predict four controlled variables (CVs): r_{cry}, v_{g}, T_{h}, and p_{mel}. We can predict p_{mel} with high accuracy if v_{g} and r_{cry} are predicted with high accuracy because p_{mel} can be calculated from the mass balance of silicon. Thus, the objective of the present study is to develop a model to accurately estimate the three CVs (r_{cry}, v_{g}, and T_{h}) from the three manipulated variables of the CZ process.

A gray-box model, which integrates the first-principle and statistical models, has been widely used in process industries [39]. The prediction accuracy of the first-principle model can be improved by updating a part of its parameters based on available data [40]. In this study, we focus on the temperature gradient at the solid-liquid interface G_{cry},

which is constant in [32] and highly affects the prediction accuracy of the CVs. Although G_{cry} cannot be measured in the real process, we calculate G_{cry} using the first-principle model and the quasi-steady-state assumption, which was used to simplify the complex differential-algebraic equations in [41]. Although the CZ process is a batch process, the operating conditions do not differ significantly from batch to batch. If the operating conditions are similar, the corresponding values of G_{cry} should also be similar. Besides, the relationship between G_{cry} and process variables is nonlinear. Based on the above considerations, we use Gaussian Process Regression (GPR) [42] as the statistical model building method. We finally build a gray-box model by integrating the first-principle model and the statistical model.

There has been another issue that the values of some of the unmeasurable variables at the start of the prediction are determined by trial-and-error, and thereby, accurate predictions can be made only in a limited period [32]. At the start of the prediction, if the crystal radius has been maintained as constant so that a cylinder suffices to describe the shape of the crystal, the quasi-steady-state assumption can be used [41]. In this study, we use data from the production of the body growth part; hence, we adopted the method of calculating the values of the unmeasured variables using the above assumption. The prediction accuracy of the proposed gray-box model and the conventional first-principle model is verified using four ingot production data.

Throughout this paper, the first-principle model consisting of an energy transfer model and a hydrodynamic and geometrical model is called the EHG model, and the proposed model is called the gray-box EHG (gray-EHG) model.

2.2 EHG model of CZ process

Figire 2.1 shows the structure of the EHG model. In the energy transfer model, the crystal growth rate v_{g} is calculated from the heater input power P, the crystal pulling

rate v_{p}, and the crucible rise rate v_{c}. In the hydrodynamic and geometrical model, the crystal radius r_{cry} at the solid-liquid interface is calculated from v_{p}, v_{c}, and v_{g}. Details of each model are given in the following sections.

2.2.1 Energy transfer model

As shown in Fig. 2.2, the CZ process is assumed to consist of nine components: a furnace wall, a crucible, a heater, a shield, a furnace bottom, melt, a meniscus section, a crystal, and an environment. The shield, the heater, and the crucible are divided into upper, middle, and lower parts. The height of each part is determined by the melt surface position and the crucible bottom position. The upper part, the middle part, and the lower part are represented by 1, 2, and 3, respectively. The energy balance of the crucible, the heater, the shield, the furnace bottom, the melt, and the meniscus section is calculated from the radiative heat transfer, conductive heat transfer, and heater input power. $Q_{i,j}$ is the radiative heat transfer from component i to component j, denoted by the solid arrow. $Q^*_{i,j}$ is the conductive heat transfer from component i to component j, indicated by the dotted arrow. Each heat transfer is calculated using the tepmerature of the components i and j. Subscripts "c," "h," "s," "b," "mel," "men," "cry," and "e" mean the crucible, the heater, the shield, the furnace bottom, the melt, the meniscus section, the crystal, and the environment, respectively. In the energy transfer model,

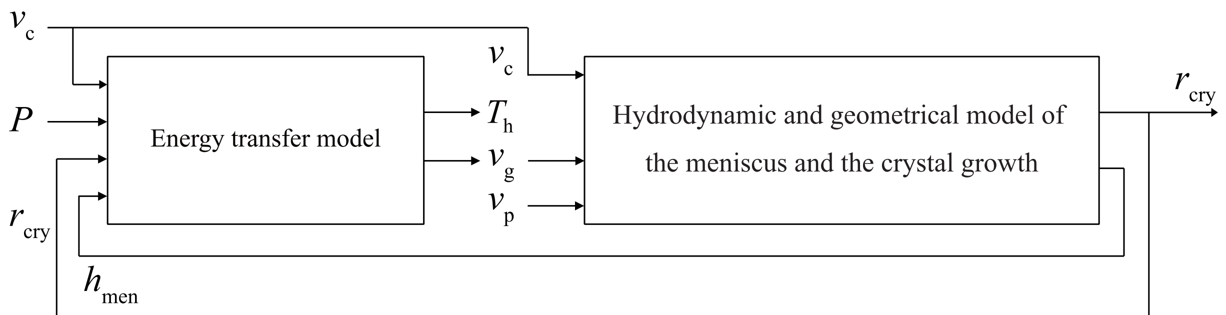

Fig. 2.1: Structure of the EHG model.

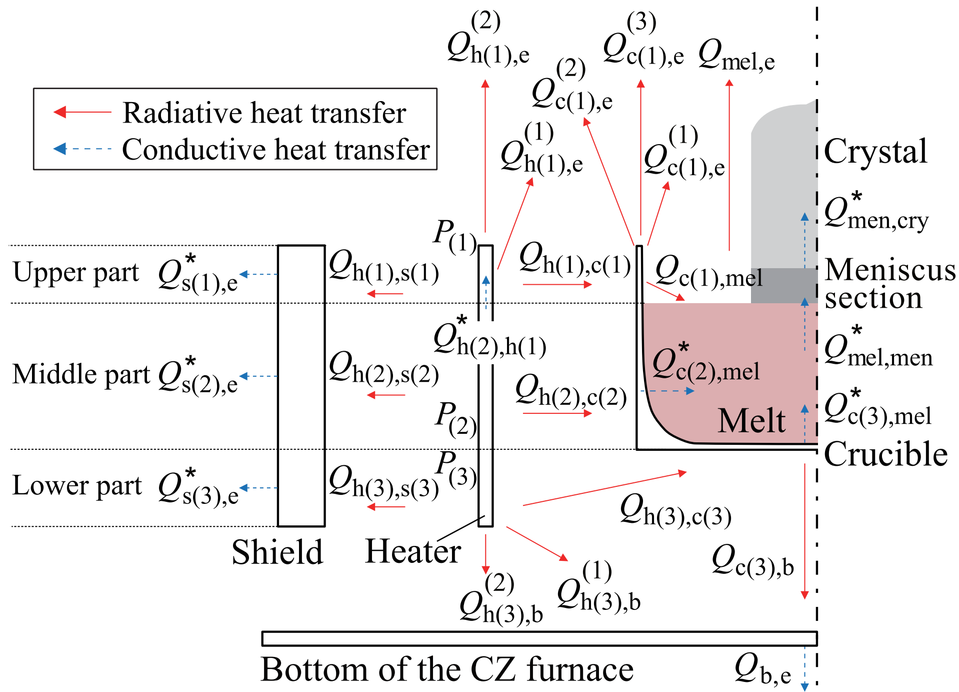

Fig. 2.2: Heat transfer calculated in the energy transfer model.

the temperature at the middle part and the lower part of the heater, $T_{h(2)}$ and $T_{h(3)}$, are the same. The variables representing the radius r and the height h of each cylindrical component of the CZ process are shown in Fig. 2.3, in which "in" and "out" represent the inside and outside parts. The amount of melt decreases with crystal growth, and the crucible rises to maintain a fixed position of the melt surface. Therefore, the upper, middle, and lower heights and the radius of the melt surface vary with the change of the melt surface position and the crucible position.

A quasi-steady state is assumed for the temperature of the shield, the crucible, and the furnace bottom to reduce the complexity and computational cost. Based on the assumption, the energy balance at the shield, the crucible, and the furnace bottom are

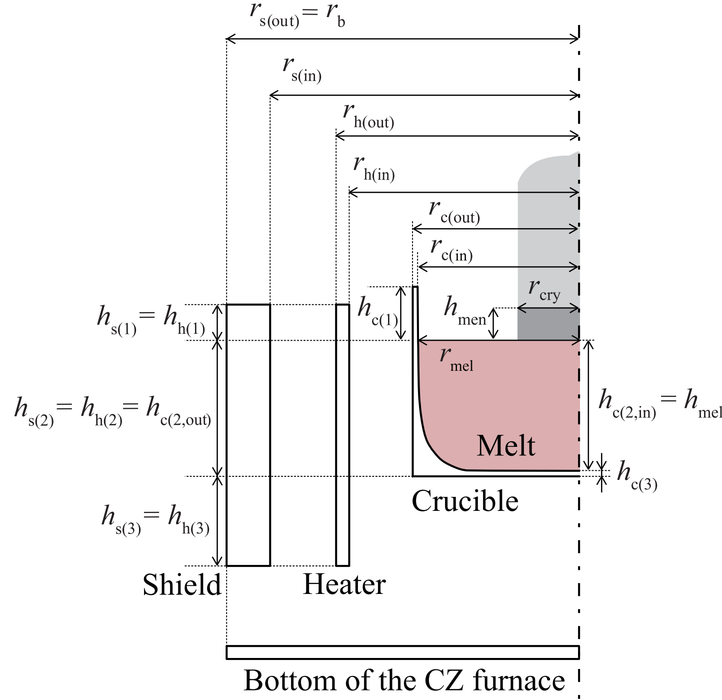

Fig. 2.3: Definition of the radius and the height of each component of the Czochralski process.

expressed by

$$Q_{\mathrm{h}(k),\mathrm{s}(k)} - Q^{*}_{\mathrm{s}(k),\mathrm{e}} = 0 \qquad (k = 1, 2, 3), \tag{2.1}$$

$$Q_{\mathrm{h}(1),\mathrm{c}(1)} - Q_{\mathrm{c}(1),\mathrm{mel}} - Q_{\mathrm{c}(1),\mathrm{e}} = 0, \tag{2.2}$$

$$Q_{\mathrm{h}(2),\mathrm{c}(2)} - Q^{*}_{\mathrm{c}(2),\mathrm{mel}} = 0, \tag{2.3}$$

$$Q_{\mathrm{h}(3),\mathrm{c}(3)} - Q^{*}_{\mathrm{c}(3),\mathrm{mel}} - Q_{\mathrm{c}(3),\mathrm{b}} = 0, \tag{2.4}$$

$$Q_{\mathrm{h}(3),\mathrm{b}} + Q_{\mathrm{c}(3),\mathrm{b}} - Q^{*}_{\mathrm{b},\mathrm{e}} = 0. \tag{2.5}$$

The energy balance of the heater is given by

$$\begin{aligned} C_{\mathrm{h}} \frac{\mathrm{d}h_{\mathrm{h}(1)} T_{\mathrm{h}(1)}}{\mathrm{d}t} &= P_{(1)} - Q_{\mathrm{h}(1),\mathrm{s}(1)} - Q_{\mathrm{h}(1),\mathrm{e}} + Q^{*}_{\mathrm{h}(2),\mathrm{h}(1)} \\ &+ C_{\mathrm{h}} \left((1 - \delta_{\mathrm{h}})\, T_{\mathrm{h}(1)} \frac{\mathrm{d}h_{\mathrm{h}(1)}}{\mathrm{d}t} + \delta_{\mathrm{h}} T_{\mathrm{h}(2)} \frac{\mathrm{d}h_{\mathrm{h}(1)}}{\mathrm{d}t} \right), \end{aligned} \tag{2.6}$$

$$
\begin{aligned}
C_{\mathrm{h}} \frac{\mathrm{d}\left(h_{\mathrm{h}(2)}+h_{\mathrm{h}(3)}\right) T_{\mathrm{h}(2)}}{\mathrm{d}t} = & \sum_{k=2}^{3}\left(P_{(k)}-Q_{\mathrm{h}(k),\mathrm{s}(k)}-Q_{\mathrm{h}(k),\mathrm{c}(k)}\right) \\
& -Q_{\mathrm{h}(2),\mathrm{h}(1)}^{*}-Q_{\mathrm{h}(3),\mathrm{b}} \\
& -C_{\mathrm{h}}\left(\left(1-\delta_{\mathrm{h}}\right) T_{\mathrm{h}(1)} \frac{\mathrm{d}h_{\mathrm{h}(1)}}{\mathrm{d}t}+\delta_{\mathrm{h}} T_{\mathrm{h}(2)} \frac{\mathrm{d}h_{\mathrm{h}(1)}}{\mathrm{d}t}\right),
\end{aligned}
\tag{2.7}
$$

$$
C_{\mathrm{h}} = c_{\mathrm{h}} \rho_{\mathrm{h}} \pi \left(r_{\mathrm{h(out)}}^{2} - r_{\mathrm{h(in)}}^{2}\right), \tag{2.8}
$$

$$
P_{(k)} = \frac{h_{\mathrm{h}(k)}}{h_{\mathrm{h}}} P = \frac{h_{\mathrm{h}(k)}}{h_{\mathrm{h}(1)}+h_{\mathrm{h}(2)}+h_{\mathrm{h}(3)}} P \quad (k=1,2,3), \tag{2.9}
$$

$$
\delta_{\mathrm{h}} = \begin{cases} 1 & \left(\frac{\mathrm{d}h_{\mathrm{h}(1)}}{\mathrm{d}t} \geq 0\right) \\ 0 & \left(\frac{\mathrm{d}h_{\mathrm{h}(1)}}{\mathrm{d}t} < 0\right) \end{cases}, \tag{2.10}
$$

where $T_{i(k)}$ is the temperature of the part i of the component k. c_{h} and ρ_{h} are the specific heat and the density of the heater.

The energy balance of the melt can be described as follows:

$$
c_{\mathrm{mel}} m_{\mathrm{mel}} \frac{\mathrm{d}T_{\mathrm{mel}}}{\mathrm{d}t} = Q_{\mathrm{c}(1),\mathrm{mel}} + Q_{\mathrm{c}(2),\mathrm{mel}}^{*} + Q_{\mathrm{c}(3),\mathrm{mel}}^{*} - Q_{\mathrm{mel,e}} - Q_{\mathrm{mel,men}}^{*}, \tag{2.11}
$$

where c_{mel}, m_{mel}, and T_{mel} are the specific capacity, the mass, and the temperature of the melt.

In the energy transfer model, the axial temperature gradient in the meniscus section is constant, and the radial temperature gradient is zero inside the meniscus section and the crystal. The crystal growth rate then can be expressed as follows from the energy

Table 2.2: Parameters used in the energy transfer model.

Variable	Description	unit	Value
$c_\mathrm{h}\rho_\mathrm{h}$	Heat capacity per unit volume of heater	J m^{-3} K^{-1}	3.6×10^6
$r_\mathrm{h(out)}$	Outer radius of heater	m	0.480
$r_\mathrm{h(in)}$	Inner radius of heater	m	0.450
h_h	Height of heater	m	0.640
c_mel	Heat capacity of melt	J kg^{-1} K^{-1}	1040
k_men	Heat conductivity of meniscus section	W m^{-1} K^{-1}	67.0
k_cry	Heat conductivity of crystal	W m^{-1} K^{-1}	21.6
ρ_cry	Density of crystal	kg m^{-3}	2330
ΔH_f	Specific latent heat of fusion for silicon	J kg^{-1} K^{-1}	1.65×10^6
T^*	Crystallization point of silicon	K	1685

balance at the solid-liquid interface between the meniscus section and the crystal:

$$v_\mathrm{g} = \frac{k_\mathrm{men}G_\mathrm{men} - k_\mathrm{cry}G_\mathrm{cry}}{\rho_\mathrm{cry}\Delta H_\mathrm{f}}, \tag{2.12}$$

$$G_\mathrm{men} = -\frac{T_\mathrm{mel} - T^*}{h_\mathrm{men}}, \tag{2.13}$$

where k_men and k_cry are the heat conductivity of the meniscus section and the crystal. G_men and G_cry are the axial thermal gradients of the meniscus section and the crystal at the solid-liquid interface, ρ_cry is the density of the crystal, and ΔH_f is the specific latent heat of fusion for silicon. T^* is the crystallization point of silicon equal to the temperature at the solid-liquid interface. In the energy transfer model, k_men, k_cry, ρ_cry, ΔH_f, T^*, and G_cry are constant. The meniscus height h_men is calculated with the hydrodynamic and geometrical model explained in Section 2.2.2.

The parameters used in the energy transfer model are shown in Table 2.2. The details of the energy transfer model are described by Zheng et al. [32].

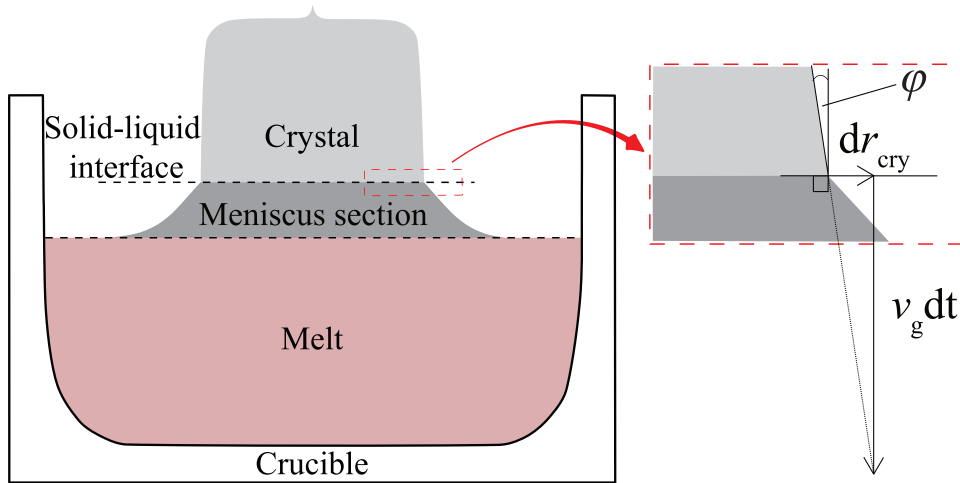

Fig. 2.4: Geometrical relationship around the solid-liquid interface.

2.2.2 Hydrodynamic and geometrical model

As shown in Fig. 2.4, r_{cry} is expressed by the following equation using v_{g} and the crystal slope angle φ [34]:

$$\frac{\mathrm{d}r_{\mathrm{cry}}}{\mathrm{d}t} = v_{\mathrm{g}} \tan(\varphi) \,. \tag{2.14}$$

Equation (2.14) denotes that φ determines the direction of change in r_{cry}, since normally $v_{\mathrm{g}} > 0$. The crystal slope angle φ is expressed by the mass balance at the meniscus as follows:

$$\frac{\mathrm{d}\varphi}{\mathrm{d}t} = \frac{v_{\mathrm{p}} - v_{\mathrm{c}} - \psi_1(r_{\mathrm{cry}}, \varphi)v_{\mathrm{g}}}{\psi_2(r_{\mathrm{cry}}, \varphi)}, \tag{2.15}$$

where ψ_1 and ψ_2 are functions of r_{cry} and φ derived from the mass balance of silicon. Details of the derivation of ψ_1 and ψ_2 are described by Winkler et al. [15]. Ferguson

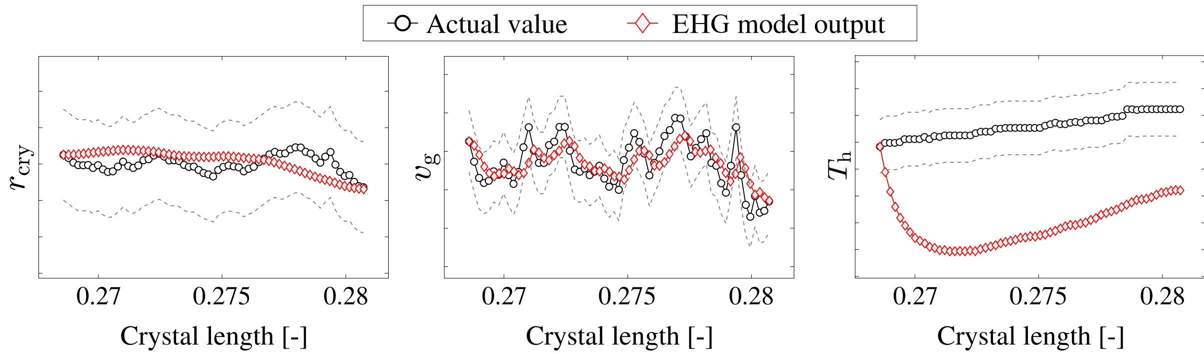

Fig. 2.5: Prediction result of the crystal radius r_{cry}, the crystal growth rate v_g, and the heater temperature T_h by the EHG model. The horizontal axis is the dimensionless crystal length. The range between the dotted lines represents the tolerance of the prediction error.

proposed describing the meniscus height h_{men} with r_{cry} and φ [43]:

$$h_{men} = a\sqrt{\frac{1-\sin(\varphi_0+\varphi)}{1+\frac{1}{\sqrt{2}r_{cry}}}}, \tag{2.16}$$

$$a = \sqrt{\frac{2\gamma}{\rho_{mel}g}}, \tag{2.17}$$

where φ_0 is the wetting angle, γ is the surface tension of silicon, and g is the gravitational acceleration.

2.2.3 Issue of EHG model

Figure 2.5 shows an example of the prediction results based on the EHG model. The heater temperature can be calculated as follows:

$$T_h = \frac{h_{h(1)}T_{h(1)} + (h_{h(2)} + h_{h(3)})T_{h(2)}}{h_{(1)} + h_{(2)} + h_{(3)}}. \tag{2.18}$$

Figure 2.5 shows that r_{cry} and v_g can be predicted with high accuracy, while T_h cannot be accurately predicted. To improve the prediction accuracy of the three CVs, we focused on the temperature gradient at the solid-liquid interface G_{cry}, which is constant

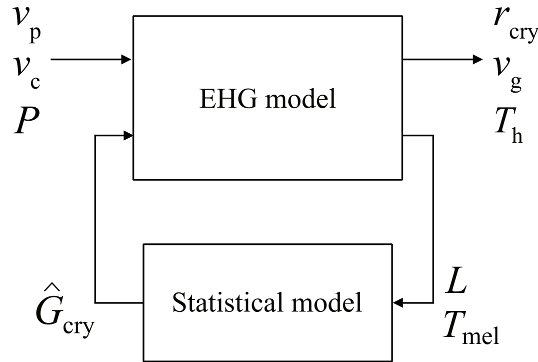

Fig. 2.6: Structure of the gray-EHG model.

in the EHG model. Rahmanpour *et al.* [28] calculated the heat flux from the interface to the crystal ϕ_s using a computational fluid dynamics simulation software CGSim [44]. They showed that ϕ_s changed with the crystal length L. The result indicates that assuming G_{cry} as a function of L will improve the prediction accuracy of the CVs, because $k_{cry}G_{cry}$ corresponds to ϕ_s and k_{cry} is constant in this study.

2.3 Proposed gray-EHG model

As shown in Fig. 2.6, the proposed model consists of the EHG model and a statistical model. We construct the statistical model to predict the temperature gradient at the solid-liquid interface G_{cry} from the crystal length L and the melt temperature T_{mel} available in real-time.

2.3.1 Training data for statistical model

Before constructing the statistical model, we generated training data of G_{cry} because G_{cry} is unmeasurable. We calculated G_{cry} using the EHG model and real process data in the following methods. We adopted a quasi-steady-state assumption [45] that the crystal length changes much slower than the temperature of each process component

and r_{cry}. This assumption leads to the following equations:

$$\frac{\mathrm{d}T_{\mathrm{h(1)}}}{\mathrm{d}t} = 0, \tag{2.19}$$

$$\frac{\mathrm{d}T_{\mathrm{h(2)}}}{\mathrm{d}t} = 0, \tag{2.20}$$

$$\frac{\mathrm{d}T_{\mathrm{mel}}}{\mathrm{d}t} = 0, \tag{2.21}$$

$$\frac{\mathrm{d}r_{\mathrm{cry}}}{\mathrm{d}t} = 0, \tag{2.22}$$

$$\frac{\mathrm{d}L}{\mathrm{d}t} = v_{\mathrm{g}}. \tag{2.23}$$

By replacing Eqs. (2.6), (2.7), and (2.11) in the energy transfer model with Eqs. (2.19)–(2.21), and using Eq. (2.22) and measurable process data (r_{cry}, v_{g}, h_{mel}, P, v_{p}, v_{c}, and crucible position p_{c}), we can calculate the temperature of each process component and φ. The following equation is obtained from Eqs. (2.12) and (2.13):

$$G_{\mathrm{cry}} = -\frac{1}{k_{\mathrm{cry}}}\left(\frac{k_{\mathrm{men}}(T_{\mathrm{mel}} - T^{*})}{h_{\mathrm{men}}} + \rho_{\mathrm{cry}}\Delta H_{\mathrm{f}} v_{\mathrm{g}}\right). \tag{2.24}$$

G_{cry} is obtained by substituting the measured values of v_{g} and r_{cry}, and the calculated values of T_{mel} and φ into Eqs. (2.16) and (2.24).

In the present study, we use real process data obtained during the production of six silicon ingots. The temperature of each process component and G_{cry} were calculated using the real process data of the ingots 1 and 2. The calculated T_{mel} and G_{cry} are shown in Fig. 2.7. The range of $k_{\mathrm{cry}}G_{\mathrm{cry}}$ calculated using CGSim by Rahmanpour *et al.* [28] is -1.24×10^{5} W/m^2 $\leq k_{\mathrm{cry}}G_{\mathrm{cry}} \leq -1.04\times10^{5}$ W/m^2, and the range of $k_{\mathrm{cry}}G_{\mathrm{cry}}$ calculated from G_{cry} shown in Fig. 2.7 is -7.6×10^{5} W/m^2 $\leq k_{\mathrm{cry}}G_{\mathrm{cry}} \leq -3.2\times10^{5}$ W/m^2. Although L and r_{cry} used by Rahmanpour et al. [28] are different from those used in the present study, $k_{\mathrm{cry}}G_{\mathrm{cry}}$ calculated from Fig. 2.7 are on the same order of that obtained by Rahmanpour et al. [28], and consequently, the derived values are considered to be reasonable.

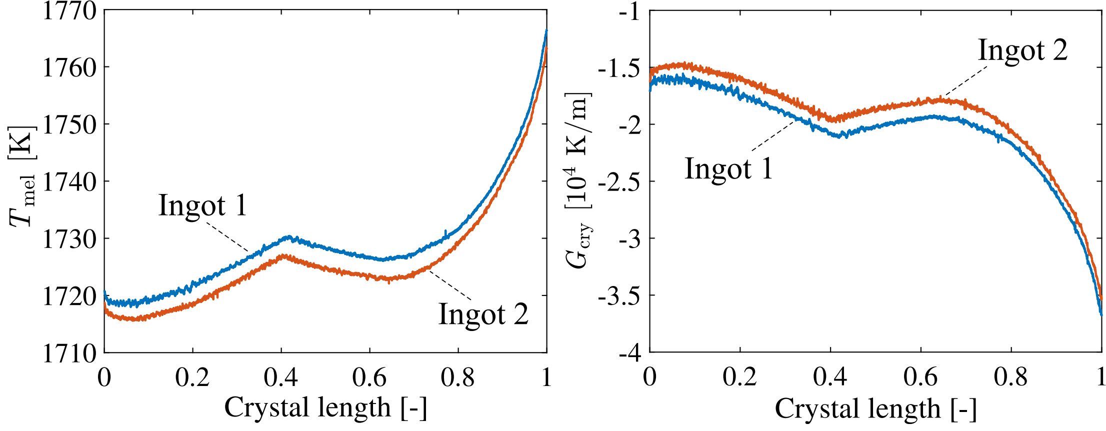

Fig. 2.7: Calculated melt temperature T_{mel} and temperature gradient in the crystal at the solid-liquid interface G_{cry} using the real process data of the ingots 1 and 2.

2.3.2 Statistical model

When predicting the CVs, we need to calculate G_{cry} from variables that are known in real-time. We, therefore, construct a statistical model whose input variables are available in real-time, and the output variable is G_{cry}. Figure 2.7 shows that G_{cry} changes with the crystal length L, but it is not uniquely determined by L. In this study, we selected L and the melt temperature T_{mel} as the input variables $\boldsymbol{x}$ of the statistical model.

We employed Gaussian Process Regression (GPR) [42]

$$y = f_{\mathrm{GPR}}(\boldsymbol{x}) + \xi, \tag{2.25}$$

where y is an output variable, and ξ is a variable that follows a Gaussian distribution with zero mean and variance σ^2, and $f_{\mathrm{GPR}}(\boldsymbol{x})$ is a latent variable from a zero-mean Gaussian process with covariance function,

$$k(\boldsymbol{x}_n, \boldsymbol{x}_{n'} \,|\, \sigma_l, \sigma_f) = \sigma_f^2 \exp\left[-\frac{1}{2}\frac{(\boldsymbol{x}_n - \boldsymbol{x}_{n'})^{\mathsf{T}}(\boldsymbol{x}_n - \boldsymbol{x}_{n'})}{\sigma_l^2}\right], \tag{2.26}$$

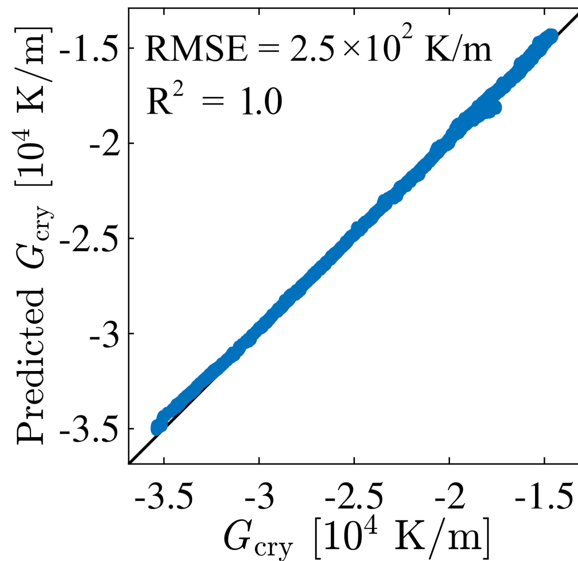

Fig. 2.8: Temperature gradient in the crystal at the solid-liquid interface G_{cry} predicted by the statistical model using the data of ingot 2.

where σ_l and σ_f are parameters, and $\boldsymbol{x}_n$ and $\boldsymbol{x}_{n'}$ are the nth and n'th samples of the input variables. In constructing the statistical model, the input and output variables were centered and scaled to have zero mean and unit variance. The parameters were determined by five-fold cross-validation.

2.3.3 Prediction accuracy of statistical model

We validated the statistical model constructed using the data of the ingot 1 by predicting G_{cry} of data of the ingot 2. The prediction results in Fig. 2.8 show that the root-mean-square error (RMSE) was 2.5×10^2 K/m, and the determination coefficient R^2 was 1.0, confirming that the developed statistical model can estimate G_{cry} with high accuracy.

2.4 Results and Discussion

The prediction accuracy of the three CVs (r_{cry}, v_{g}, and T_{h}) by the EHG model and the proposed gray-EHG model was compared using real process data.

2.4.1 Simulation Conditions

To compare the prediction accuracy under different operating conditions, we applied the models to data of the ingots 3 to 6 that were obtained during the production of the ingot body. The data were divided without duplication into hourly subdata, and a total of 328 subdata (82 subdata per ingot) were used for validation. Both models require the initial values of four variables: the crystal slope angle φ, the temperature at the upper part of the heater $T_{\mathrm{h}(1)}$, the temperature at the middle part of the heater $T_{\mathrm{h}(2)}$, and the melt temperature T_{mel}. In the previous study [32], the initial values were determined by trial and error to minimize the prediction error because a systematic method for determining the initial values had not been developed. In this research, the initial values were calculated by the same method described in Section 2.3.1. In the EHG model, G_{cry} was calculated using Eq. (2.24) and process data (v_{g}, T_{mel}, and h_{men}) at the start of the prediction.

2.4.2 Prediction results

The statistical model in the proposed gray-EHG model was constructed using the training data generated from the data of the ingots 1 and 2. The parameters were determined by five-fold cross-validation; $\sigma = 0.01$, $\sigma_l = 5.43$, and $\sigma_f = 4.84$. The prediction accuracy of the CVs was evaluated based on the RMSE scaled by the acceptable error. Figure 2.9 shows the RMSE of each subdata against the crystal length at the start of the prediction. Figure 2.10 shows the prediction results of the CVs at three stages in the data of the ingot 3. Table 2.3 shows that the mean value and standard deviation of the RMSEs of the gray-EHG model are smaller than those of the EHG model in all cases. The proposed gray-EHG model reduced the mean of RMSEs of r_{cry}, v_{g}, and T_{h} by 93.7–94.4%, 56.2–69.2%, and 56.8–84.4%, respectively, compared to the EHG model.

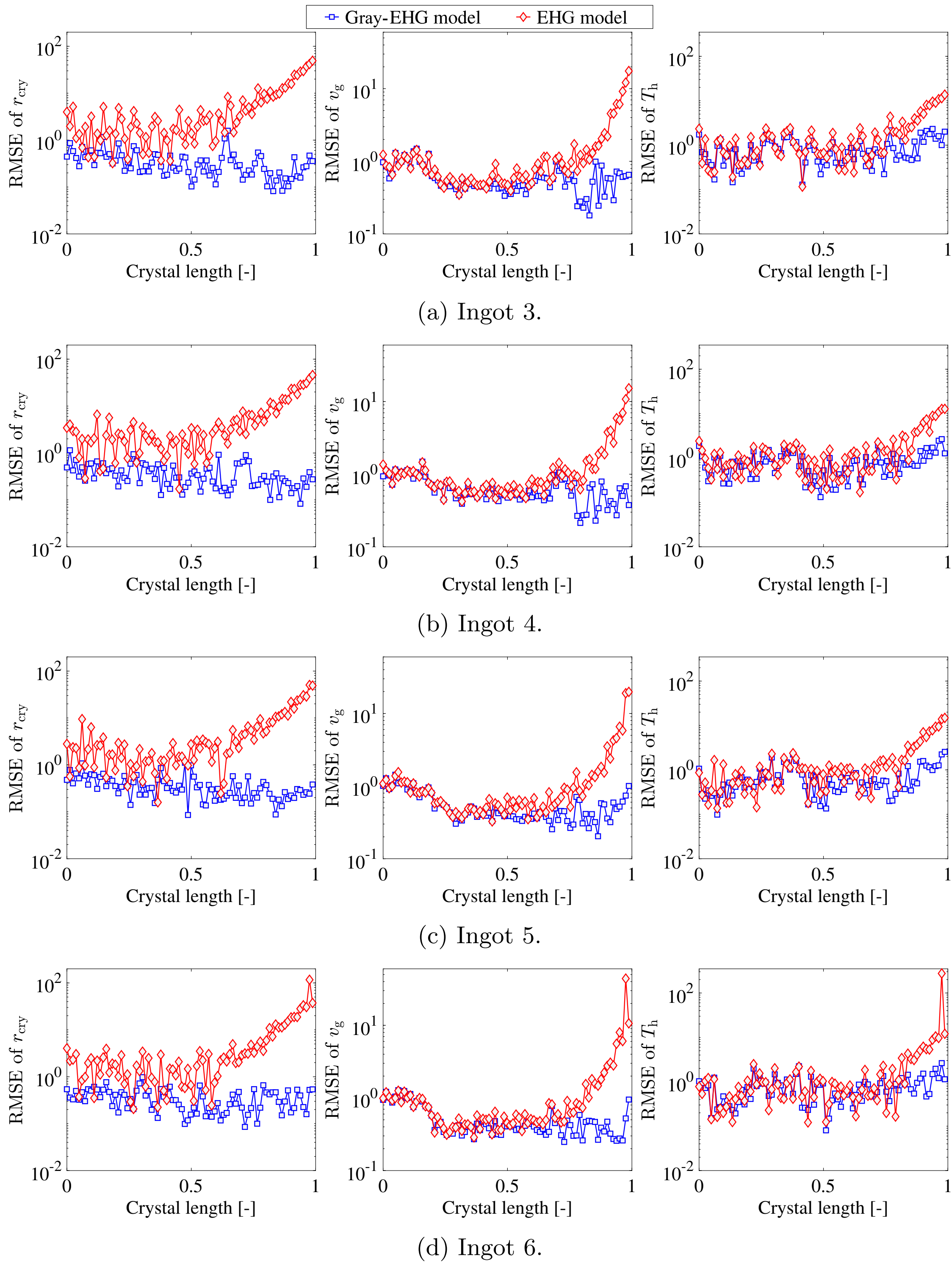

Fig. 2.9: RMSEs of the crystal radius r_{cry}, the crystal growth rate v_{g}, and the heater temperature T_{h} against the data of the ingots 3 to 6. The horizontal axis is the dimensionless crystal length.

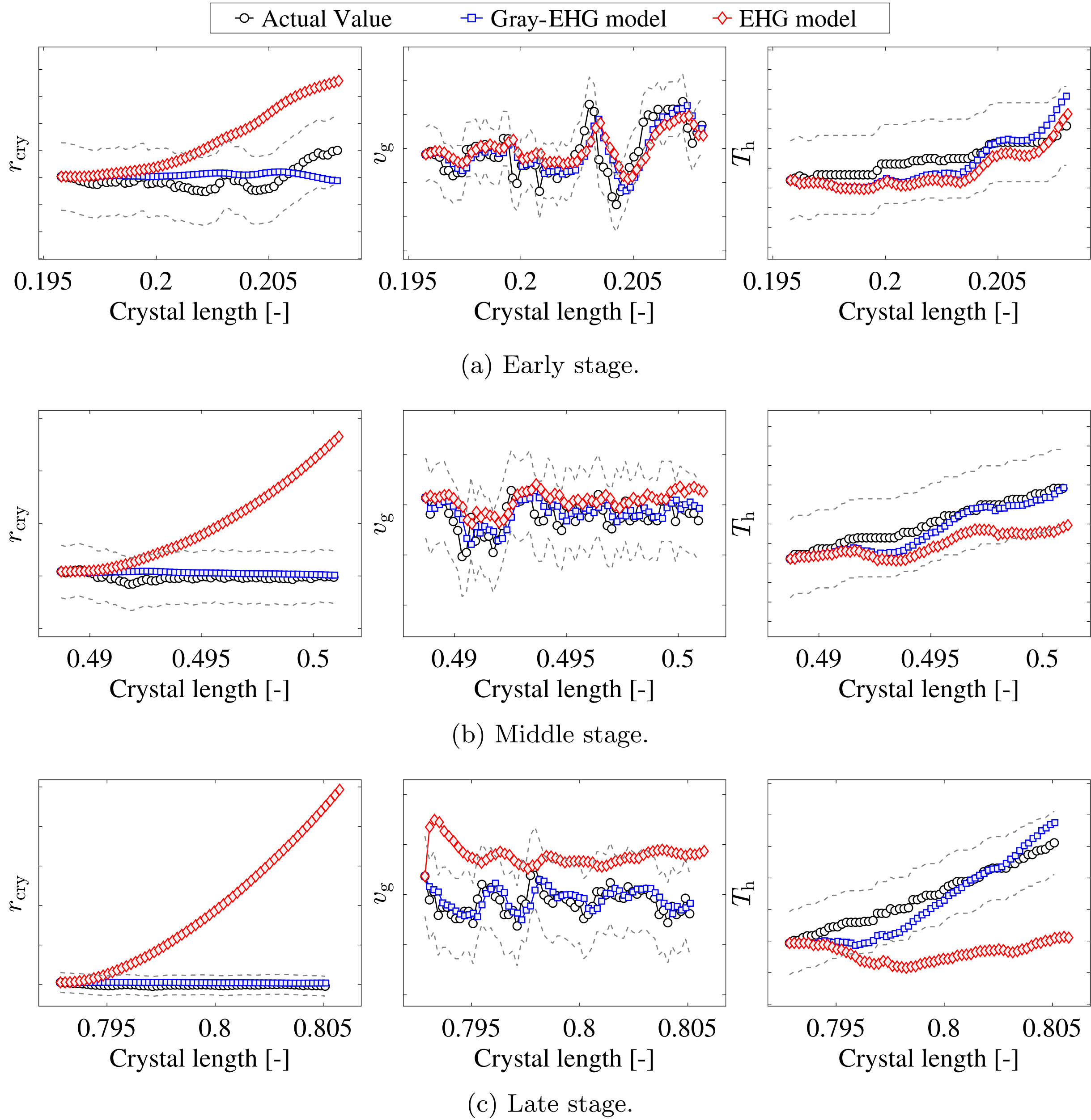

(a) Early stage.

(b) Middle stage.

(c) Late stage.

Fig. 2.10: Prediction results of the crystal radius r_{cry}, the crystal growth rate v_g, and the heater temperature T_h at three stages in data of the ingot 3. The range between the dotted lines shows an acceptable error.

2.4.3 Discussion

The EHG model can accurately predict r_{cry} and v_{g} when the initial values of the four variables (φ, $T_{\mathrm{h}(1)}$, $T_{\mathrm{h}(2)}$, and T_{mel}) were determined by trial and error as shown in Fig. 2.5. The initial values were calculated by the method described in section 2.3.1; hence, the prediction accuracy of the EHG model was decreased for r_{cry} and v_{g}. On the other hand, the gray-EHG model can accurately predict the three CVs. Figure 2.11 shows that G_{cry} changes by about 1% in an hour in the gray-EHG model. These results show that predicting the change in G_{cry} based on the operating conditions is essential to achieve high prediction accuracy of the CVs. The prediction accuracy was significantly improved at the late stage, where the change of G_{cry} against the crystal length is larger than that at the other stages.

2.5 Conculusion

We developed a gray-box model that predicts the three CVs (r_{cry}, v_{g}, and T_{h}) with high accuracy, because the conventional first-principle model was not accurate enough

Table 2.3: The mean and standard deviation of the RMSEs of three controlled variables: the crystal radius r_{cry}, the crystal growth rate v_{g}, and the heater temperature T_{h}.

Ingot	Model	RMSE of r_{cry}		RMSE of v_{g}		RMSE of T_{h}	
		mean	std	mean	std	mean	std
3	gray-EHG	0.38	0.21	0.64	0.25	0.83	0.53
	EHG	6.1	8.8	1.5	2.2	1.9	2.6
4	gray-EHG	0.37	0.25	0.61	0.27	0.86	0.54
	EHG	6.3	9.5	1.5	2.6	2.1	1.0×10^{6}
5	gray-EHG	0.37	0.21	0.55	0.27	0.69	0.51
	EHG	5.9	9.5	1.5	3.1	1.9	2.8
6	gray-EHG	0.36	0.18	0.51	0.26	0.78	0.50
	EHG	6.3	15	1.7	5.0	5.0	30

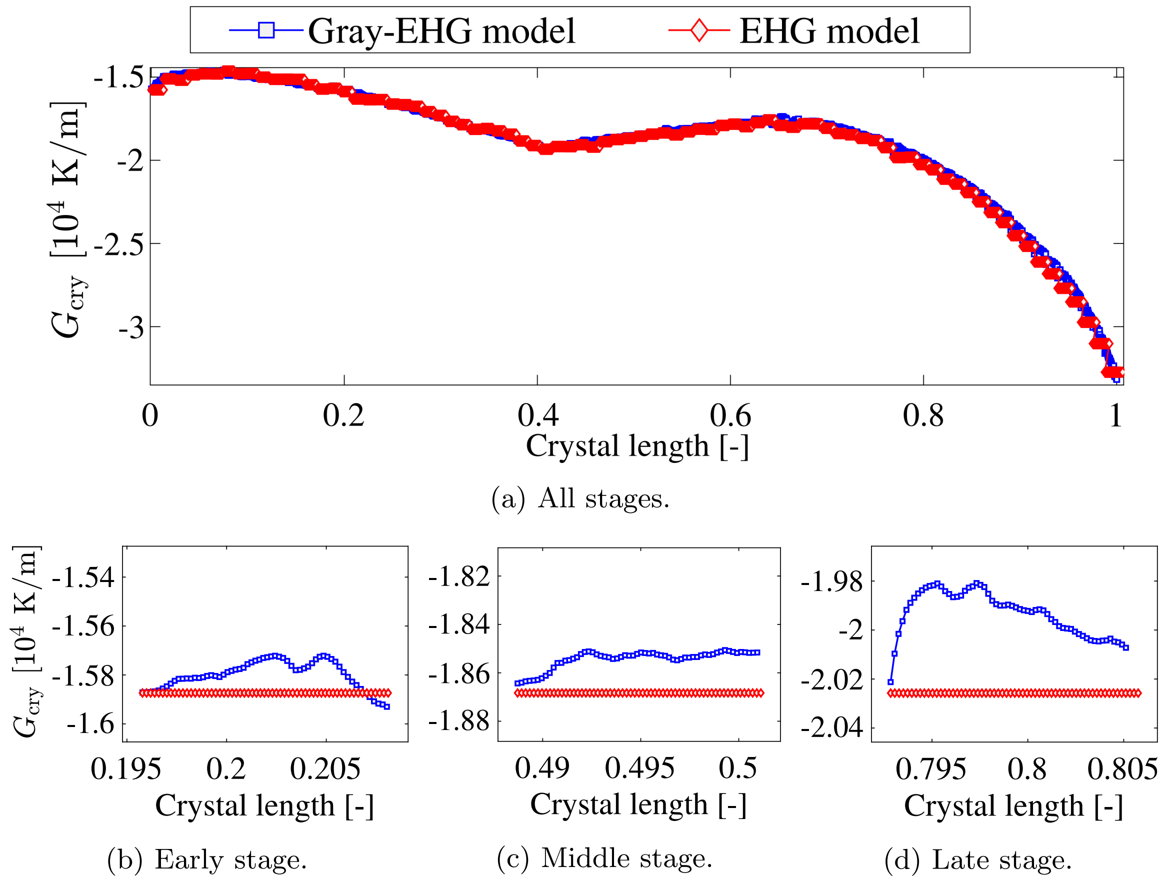

(a) All stages.

(b) Early stage. (c) Middle stage. (d) Late stage.

Fig. 2.11: Temperature gradient in the crystal at the solid-liquid interface G_{cry} used for prediction in the data of the ingot 3 by the EHG model and the gray-EHG model.

to predict T_h. In the gray-box model, a statistical model is employed to predict the temperature gradient in the crystal at the solid-liquid interface G_{cry} from the crystal length L and the melt temperature T_{mel}. The gray-box model and the first-principle model were validated using real process data. The gray-box model reduced the RMSEs of r_{cry}, v_g, and T_h by 94.1%, 62.7%, and 70.6%, compared to the first-principle model. A significant improvement in prediction accuracy was achieved, especially for the late phase of the batch, where G_{cry} changes faster than the other phases.

Chapter 3

Gray-box model-based predictive control

3.1 Introduction

Table 3.1 summarizes previous research on MPC of the CZ process. Irizarry-Rivera and Seider [25, 26] developed two model predictive controllers: one controls r_{cry} by manipulating v_{p}, and the other controls v_{p} by manipulating P. Abdollahi et al. [27] derived the optimal temperature trajectory using quadratic programming and then implemented an MPC strategy to track the optimal temperature. Rahmanpour et al. [28] developed a control strategy with two model predictive controllers to control r_{cry} and melt temperature T_{mel}. Liu et al. [30] proposed a control structure where r_{cry} is controlled by manipulating T_{h} with constant v_{p}. Lee et al. [17] and Zhang et al. [18] used MPC to determine a feedforward trajectory of temperature in the traditional control structure.

As shown in Table 3.1, two of seven studies focused on the commercial CZ process producing 300 mm silicon ingots. Although control of r_{cry}, v_{g}, and p_{mel} is required to manufacture high-quality products, p_{mel} is not used as the CV in the previous studies. Besides, in four of seven previous studies, v_{p} is controlled instead of v_{g}. The reason

Table 3.1: Research on MPC of the CZ process.

Reference	Controlled variable	Manipulated variable	Crystal diameter [mm]
[25, 26]	r_{cry} v_{p}	v_{p} P	40
[27]	r_{cry}, T_{h}	P, v_{p}	50
[28]	r_{cry}, T_{mel}	P, v_{p}	160
[30]	r_{cry}, T_{h}	T_{h}	208
[18]	r_{cry}, T_{h}, v_{p}	P, v_{p}	300
[17]	r_{cry}, T_{h}, v_{p}	P, v_{p}	300
Present study	r_{cry}, v_{g}, p_{mel}	P, v_{p}, v_{c}	300

would be there had been no model predicting the three variables (r_{cry}, v_{g}, and p_{mel}) with high accuracy. Zheng et al. [32] developed a first-principle model to predict r_{cry} and v_{g} from P, v_{p}, and v_{c} in the process producing 300 mm silicon ingots. We improved the first-principle model and built a gray-box (GB) model to predict all CVs used in the industrial process as shown in Chapter 2. The present chapter proposes an MPC method based on the GB model. Although the GB model can accurately predict the CVs, solving an optimization problem using the GB model requires a high computational cost. To reduce the computational cost, we apply successive linearization proposed by Megías et al. [33] and simplify the optimization problem. Our contributions are summarised as follows:

- Develop an MPC method based on the gray-box model predicting three CVs with high accuracy.
- Improve disturbance rejection performance than the conventional control method even when a plant-model mismatch exists.

This chapter proposes a model-based predictive control method with higher control performance than the conventional method using PID controllers; thus, we need a model that can accurately predict the CVs of the industrial CZ process. The GB model

in Chapter 2 satisfies this requirement and does not require further improvement in prediction accuracy for the purpose.

3.2 Proposed control method

The CVs and the manipulated variables (MVs) are defined as follows:

$$\boldsymbol{y}(t) = [r_{\mathrm{cry}}(t),\ v_{\mathrm{g}}(t),\ p_{\mathrm{mel}}(t)]^{\mathsf{T}}, \tag{3.1}$$

$$\boldsymbol{u}(t) = [P(t),\ v_{\mathrm{p}}(t),\ v_{\mathrm{c}}(t)]^{\mathsf{T}}. \tag{3.2}$$

Here, the number of the MVs and the CVs n_u and n_y are three. MPC requires predictions of $\boldsymbol{y}(t)$ over the prediction horizon ($t = t_0 + 1, \cdots, t_0 + H_{\mathrm{p}}$) at each sampling instant t_0. The proposed method computes the output predictions $\hat{\boldsymbol{y}}$ expressed as

$$\hat{\boldsymbol{y}}(t) = \hat{\boldsymbol{y}}_{\mathrm{free}}(t) + \hat{\boldsymbol{y}}_{\mathrm{forced}}(t), \tag{3.3}$$

where $\hat{\boldsymbol{y}}_{\mathrm{free}}$ is a free response, which is an output of the GB model without change in input variables ($\Delta\boldsymbol{u}(t) = \boldsymbol{u}(t) - \boldsymbol{u}(t-1) = 0$) over the prediction horizon. $\hat{\boldsymbol{y}}_{\mathrm{forced}}$ is a forced response, which depends on $\Delta\boldsymbol{u}(t)$ over the prediction horizon. Successive linearization of the GB model is applied and a state-space model computing $\hat{\boldsymbol{y}}_{\mathrm{forced}}$ is derived every linearization interval Δt_{l} to solve the optimization problem in several seconds. The next MVs $\boldsymbol{u}(t_0)$ are determined by solving the optimization problem in 3.2.2 for each control interval Δt_{c}.

3.2.1 Successive linearization

It is challenging to linearize the GB model analytically because the GB model has several nonlinear algebraic equations, including a term of radiation heat transfer proportional to the fourth power of the component's temperature. Based on the method developed

by Megías et al. [33], the GB model is linearized in the following steps:

1. Calculate a free response $\hat{\boldsymbol{y}}_{\text{free}}(t)$ over the prediction horizon by the GB model with $\boldsymbol{u}(t) = \boldsymbol{u}(t_0 - 1)$.
2. For $i = 1$, 2, and 3, calculate $\hat{\boldsymbol{y}}_{u_i}(t)$, which is an output of the GB model over the prediction horizon with

$$u_j(t) = \begin{cases} u_j(t_0 - 1) + \Delta u_{j,\max} & (j = i), \\ u_j(t_0 - 1) & (j \neq i), \end{cases} \tag{3.4}$$

   where u_j is the jth variable in (3.2), and $\Delta u_{j,\max}$ is the maximum absolute change of u_j in one-batch operation data obtained from the industrial process.
3. For $i = 1$, 2, and 3, calculate difference between the responses $\hat{\boldsymbol{y}}_{u_i}(t)$ and $\hat{\boldsymbol{y}}_{\text{free}}(t)$ given by

$$\boldsymbol{Y}_{u_i} = \begin{bmatrix} \left(\hat{\boldsymbol{y}}_{u_i}(t_0 + 1) - \hat{\boldsymbol{y}}_{\text{free}}(t_0 + 1)\right)^\top \\ \left(\hat{\boldsymbol{y}}_{u_i}(t_0 + 2) - \hat{\boldsymbol{y}}_{\text{free}}(t_0 + 2)\right)^\top \\ \vdots \\ \left(\hat{\boldsymbol{y}}_{u_i}(t_0 + H_{\text{p}}) - \hat{\boldsymbol{y}}_{\text{free}}(t_0 + H_{\text{p}})\right)^\top \end{bmatrix}. \tag{3.5}$$

4. Derive a state-space model

$$\hat{\boldsymbol{y}}_{\text{forced}}(t) = \boldsymbol{C}\boldsymbol{x}(t), \tag{3.6}$$

$$\boldsymbol{x}(t + 1) = \boldsymbol{A}\boldsymbol{x}(t) + \boldsymbol{B}\Delta\boldsymbol{u}(t), \tag{3.7}$$

   where $\boldsymbol{A}$, $\boldsymbol{B}$, and $\boldsymbol{C}$ are matrices calculated from $\boldsymbol{Y}_{u_1}$, $\boldsymbol{Y}_{u_2}$, and $\boldsymbol{Y}_{u_3}$, and $\boldsymbol{x}$ is a state vector.

Details of the derivation of the state-space model are described by Jimoh and Dan' Isa [46].

3.2.2 Optimization problem of model predictive control

For each control interval, the optimal MVs $\boldsymbol{u}_{\mathrm{opt}}(t)$ over the control horizon ($t = t_0, \cdots, t_0 + H_{\mathrm{c}} - 1$) are obtained by solving the following optimization problem:

$$\min_{\boldsymbol{u}(t)\ (t=t_0,\cdots,t_0+H_{\mathrm{c}}-1)} \sum_{t=t_0+1}^{t_0+H_{\mathrm{p}}} \boldsymbol{e}(t)^{\mathsf{T}} \boldsymbol{Q} \boldsymbol{e}(t) + \sum_{t=t_0}^{t_0+H_{\mathrm{c}}-1} \Delta \boldsymbol{u}(t)^{\mathsf{T}} \boldsymbol{R} \Delta \boldsymbol{u}(t), \tag{3.8}$$

$$\text{s.t.} \quad \boldsymbol{e}(t) = \boldsymbol{y}_{\mathrm{set}}(t) - \hat{\boldsymbol{y}}(t), \tag{3.9}$$

$$\hat{\boldsymbol{y}}(t) = \hat{\boldsymbol{y}}_{\mathrm{free}}(t) + \hat{\boldsymbol{y}}_{\mathrm{forced}}(t), \tag{3.10}$$

$$\hat{\boldsymbol{y}}_{\mathrm{forced}}(t) = \boldsymbol{C}\boldsymbol{x}(t), \tag{3.11}$$

$$\boldsymbol{x}(t+1) = \boldsymbol{A}\boldsymbol{x}(t) + \boldsymbol{B}\Delta\boldsymbol{u}(t), \tag{3.12}$$

$$\boldsymbol{x}(t_0) = \boldsymbol{0}, \tag{3.13}$$

$$\Delta\boldsymbol{u}_{\min} \leq \Delta\boldsymbol{u}(t) \leq \Delta\boldsymbol{u}_{\max}, \tag{3.14}$$

$$\boldsymbol{u}(t) \geq \boldsymbol{0}, \tag{3.15}$$

$$\Delta\boldsymbol{u}(t) = \boldsymbol{0} \quad (t = t_0 + H_{\mathrm{c}}, \cdots, t_0 + H_{\mathrm{p}} - 1), \tag{3.16}$$

where $\boldsymbol{Q}$ and $\boldsymbol{R}$ are diagonal weighting matrices. H_{c} and H_{p} are the lengths of the control horizon and the prediction horizon. $\Delta\boldsymbol{u}_{\max}$ is a vector whose ith element is $\Delta u_{i,\max}$, and $\Delta\boldsymbol{u}_{\min}$ is a vector whose ith element is $-\Delta u_{i,\max}$. The next MVs are the optimal MVs at $t = t_0$: $\boldsymbol{u}(t_0) = \boldsymbol{u}_{\mathrm{opt}}(t_0)$.

3.3 Simulation condition

We evaluated the disturbance rejection performance of the conventional and proposed methods through control simulations in the following procedure:

1. Control the process by the conventional method until relative control deviations of all CVs to $\epsilon_{y_i,\max}$ are smaller than 0.01 during 10 minutes.
2. Switch the control method to the proposed one when evaluating the performance of the proposed method.
3. Control the process for 30 minutes without disturbance.
4. After the 30 minutes, inject a constant disturbance during a minute into one of the MVs or the CVs except for v_{g}. The magnitude of the disturbance to the MV and the CV is $\Delta u_{i,\max}$ and $\epsilon_{y_i,\max}$, respectively.
5. Continue the simulation for the next 120 minutes.

$\epsilon_{y_i,\max}$ is the maximum absolute control deviation of the ith CV y_i in one-batch industrial process data.

The dynamic characteristics of the CZ process change as the crystal grows; thus, we compared the performance at the early, middle, and late stages. Each of them corresponds to the stage where the crystal length is 0–33%, 33–66%, and 66–100% of the product's crystal length.

We used the GB model as the controlled process. In the proposed method, the control simulations with or without a plant-model mismatch were conducted. In cases with a plant-model mismatch, two types of mismatches were used. The plant-model mismatch was represented by changing the physical property in the prediction model. The values of most of the physical properties used in the gray-box model were provided by SUMCO Corporation. On the other hand, the two physical property values, the overall heat transfer coefficient of the heater U_{h} and the melt emissiity $\varepsilon_{\mathrm{mel}}$, in the prediction model may differ significantly from their true values. This is because the true value of U_{h} is unknown and $\varepsilon_{\mathrm{mel}}$ is between 0.2 and 0.3 in previous studies [32, 34, 47, 48]. In the controlled process, U_{h} and $\varepsilon_{\mathrm{mel}}$ were 490 W/(m^{2}K) and 0.25. In the prediction model, U_{h} was changed to $490\times1.1 = 539$ W/(m^{2}K) or $\varepsilon_{\mathrm{mel}}$ was changed to $0.25\times0.95 = 0.2375$.

In the conventional method, the PID controllers were designed using the improved,

simplified internal model control (SIMC) tuning rules [49]. The control interval of the conventional method is 1 s. In the proposed method, $\Delta t_{\mathrm{c}} = \Delta t_{\mathrm{l}} = 1$ min, $H_{\mathrm{p}} = 60$ min, and $H_{\mathrm{c}} = 10$ min. The weighting matrices were as follows:

$$\boldsymbol{Q} = \mathrm{diag}\left(\frac{100}{\epsilon_{y_1,\max}}, \frac{100}{\epsilon_{y_2,\max}}, \frac{100}{\epsilon_{y_3,\max}}\right), \tag{3.17}$$

$$\boldsymbol{R} = \mathrm{diag}\left(\frac{1}{\Delta u_{1,\max}}, \frac{1}{\Delta u_{2,\max}}, \frac{1}{\Delta u_{3,\max}}\right). \tag{3.18}$$

H_{p}, H_{c}, $\boldsymbol{Q}$, and $\boldsymbol{R}$ were determined to minimize the sum of the integral absolute errors (IAEs) of the three CVs through prior several control simulations. The differences between the control simulations and the real control are summarized in Table 3.2.

3.4 Results

3.4.1 Linearization of gray-box model

Figure 3.1 shows $\boldsymbol{Y}_{u_i}$ used in procedure 3 in section 3.2.1 during control simulations without a plant-model mismatch. The values of u_i and y_i are nondimensionalized by scaling factors $\Delta u_{i,\max}$ and $\epsilon_{y_i,\max}$, respectively. Note that the values of the scaling factors affect the changes in the CVs.

The input-output relationships between P and the CVs (b–d), v_{p} and r_{cry} (f), and v_{c} and r_{cry} (j) change with time more significantly than the others. The change in r_{cry} 60

Table 3.2: Differences between the control simulations and the real control.

	Control simulations		Real control
	MPC	PID	PID
Controlled process	Gray-box model		Real process
Control interval	60 sec	1 sec	—
Tuning method	Minimizing sum of IAEs of controlled variables	Improved SIMC tuning rules	—
Controlled variables	r_{cry}, v_{g}, p_{mel}	r_{cry}, p_{mel}, T_{h}	

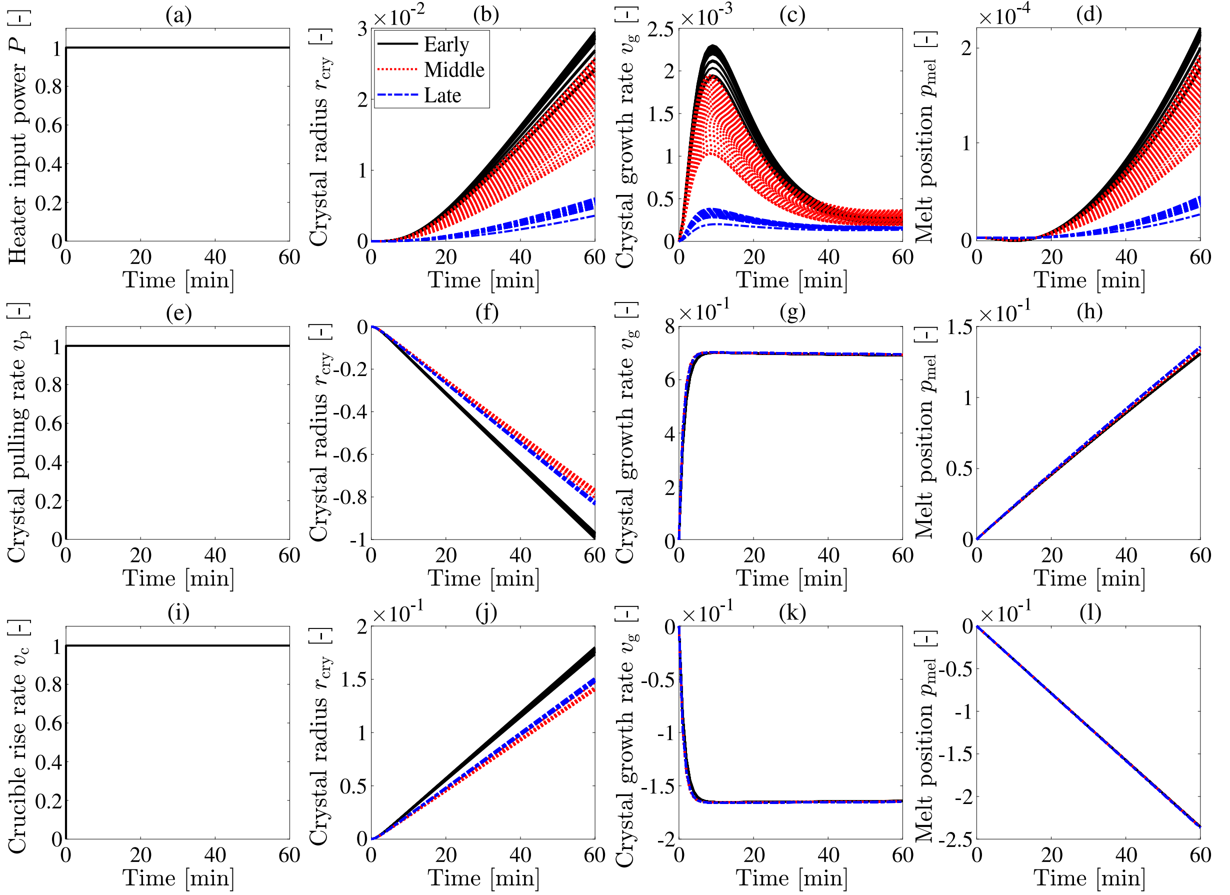

Fig. 3.1: Responses used for linearization. Responses with steps of (a) P, (b) v_{p}, and (c) v_{c} are shown in (b)–(d), (f)–(h), (j)–(l), respectively. 30 responses are plotted at each stage.

minutes after the step change in v_{p} and v_{c} at the early stage is about 20% larger than that at the other stages. This is because v_{g} at the early stage is smaller than that at the other stages; when v_{g} becomes small, the change in φ becomes large, and consequently the change in r_{cry} becomes large as shown in Eqs. (2.14) and (2.15). Successive linearization is required to represent these time-varying input-output relationships in a prediction model.

The changes in the CVs 60 minutes after the step change in v_{p} and v_{c} are 5 (b and j) to 1000 (d and l) times larger than those after the step change in P. This result is qualitatively consistent with the fact that v_{p} and v_{c} are mainly used to control r_{cry}

Table 3.3: IAEs of controlled variables in the presence of disturbance in early stage.

Case	VWD[a]	CPP[b]	r_{cry}		v_{g}		p_{mel}		Sum	
			MPC	PID	MPC	PID	MPC	PID	MPC	PID
1	P	-	0.10	1.3	1.1	3.0	0.020	0.52	1.2	4.8
2		U_{h}	0.12		1.2		0.020		1.3	
3		$\varepsilon_{\mathrm{mel}}$	0.11		1.1		0.020		1.2	
4	v_{p}	-	0.57	2.1	3.6	4.5	0.056	0.76	4.2	7.3
5		U_{h}	0.56		3.5		0.057		4.1	
6		$\varepsilon_{\mathrm{mel}}$	0.58		3.6		0.054		4.2	
7	v_{c}	-	0.33	1.5	2.9	3.1	0.17	1.9	3.4	6.6
8		U_{h}	0.35		2.9		0.18		3.5	
9		$\varepsilon_{\mathrm{mel}}$	0.33		2.8		0.17		3.3	
10	r_{cry}	-	0.94	2.4	4.9	4.1	0.27	0.53	6.1	7.1
11		U_{h}	0.90		4.8		0.27		5.9	
12		$\varepsilon_{\mathrm{mel}}$	1.1		5.5		0.27		6.9	
13	p_{mel}	-	0.52	1.3	3.0	3.0	0.23	1.7	3.8	6.0
14		U_{h}	0.52		3.1		0.23		3.9	
15		$\varepsilon_{\mathrm{mel}}$	0.53		3.1		0.23		3.8	

[a] Variable with disturbance
[b] Changed physical property

in the industrial CZ process. Since v_{c} highly affects the CVs, it should be essential to manipulate v_{c} to achieve high control performance.

3.4.2 Control simulation

The IAEs of the conventional method (PID) and the proposed method (MPC) are shown in Tables 3.3–3.5, where the IAE of y_i is nondimensionalized by $\epsilon_{y_i,\max}$. In the cases without a plant-model mismatch, the sum of IAEs of MPC is 11–87% of that of PID. In the cases with a plant-model mismatch, the sum of IAEs of MPC is 11–98% of that of PID. MPC achieved better disturbance rejection performance than PID even when a 5% or 10% plant-model mismatch exists. Quad-Core Intel Core i5 CPU (2.3 GHz) was used, and it took less than 30 seconds to compute MVs at each control interval (60

Table 3.4: IAEs of controlled variables in the presence of disturbance in middle stage.

Case	VWD[a]	CPP[b]	r_{cry}		v_{g}		p_{mel}		Sum	
			MPC	PID	MPC	PID	MPC	PID	MPC	PID
16	P	-	0.23	5.7	1.5	4.9	0.0065	0.030	1.7	11
17		U_{h}	0.20		1.4		0.0069		1.6	
18		$\varepsilon_{\mathrm{mel}}$	0.30		1.6		0.0054		1.9	
19	v_{p}	-	0.73	6.1	3.9	6.6	0.047	0.53	4.7	13
20		U_{h}	0.70		3.9		0.048		4.7	
21		$\varepsilon_{\mathrm{mel}}$	0.82		3.9		0.046		4.8	
22	v_{c}	-	0.46	5.8	3.2	5.0	0.16	1.9	3.8	13
23		U_{h}	0.44		3.2		0.16		3.8	
24		$\varepsilon_{\mathrm{mel}}$	0.55		3.2		0.16		3.9	
25	r_{cry}	-	1.7	6.8	7.1	6.3	0.26	0.051	9.1	13
26		U_{h}	1.7		7.1		0.28		9.0	
27		$\varepsilon_{\mathrm{mel}}$	1.6		6.3		0.22		8.1	
28	p_{mel}	-	0.54	5.7	3.4	4.9	0.22	1.1	4.2	12
29		U_{h}	0.52		3.3		0.22		4.1	
30		$\varepsilon_{\mathrm{mel}}$	0.60		3.5		0.22		4.3	

[a] Variable with disturbance
[b] Changed physical property

seconds).

The control simulation results in cases 19–21 are shown in Fig. 3.2. Each vertical axis of the MVs and the CVs is nondimensionalized by $\Delta u_{i,\max}$ and $\epsilon_{y_i,\max}$, respectively, and scaled so that each initial value in the conventional method is zero. Even with a 10% plant-model mismatch, MPC reduced the control deviation of r_{cry} and p_{mel} much faster than PID.

3.5 Conclusion

We proposed a nonlinear model predictive control method based on successive linearization of the gray-box model of the Czochralski process. The proposed method's control

Table 3.5: IAEs of controlled variables in the presence of disturbance in late stage.

Case	VWD[a]	CPP[b]	r_{cry}		v_g		p_{mel}		Sum	
			MPC	PID	MPC	PID	MPC	PID	MPC	PID
31		-	0.26		1.7		0.014		2.0	
32	P	U_h	0.25	3.5	1.7	2.0	0.014	13	2.0	18
33		ε_{mel}	0.26		1.7		0.014		2.0	
34		-	0.68		4.1		0.048		4.8	
35	v_p	U_h	0.66	3.9	4.0	2.4	0.047	13	4.8	19
36		ε_{mel}	0.69		4.1		0.048		4.8	
37		-	0.45		3.4		0.16		4.0	
38	v_c	U_h	0.44	3.4	3.4	2.9	0.16	15	4.0	21
39		ε_{mel}	0.46		3.4		0.16		4.0	
40		-	1.4		7.0		0.30		8.7	
41	r_{cry}	U_h	1.3	3.3	6.5	2.3	0.27	13	8.0	18
42		ε_{mel}	1.4		6.8		0.26		8.4	
43		-	0.63		3.8		0.23		4.6	
44	p_{mel}	U_h	0.61	3.5	3.8	2.4	0.23	14	4.6	20
45		ε_{mel}	0.63		3.8		0.23		4.6	

[a] Variable with disturbance
[b] Changed physical property

performance was compared with that of the conventional method using PID controllers through control simulations. The results demonstrated that the proposed method provided a higher disturbance rejection performance than the conventional method in the cases with or without a 5% or 10% plant-model mismatch. The sum of integral absolute errors of the controlled variables of the proposed method was 11–98% of that of the conventional method. Besides, the proposed method was able to calculate the MVs in a sufficiently shorter time than the control interval.

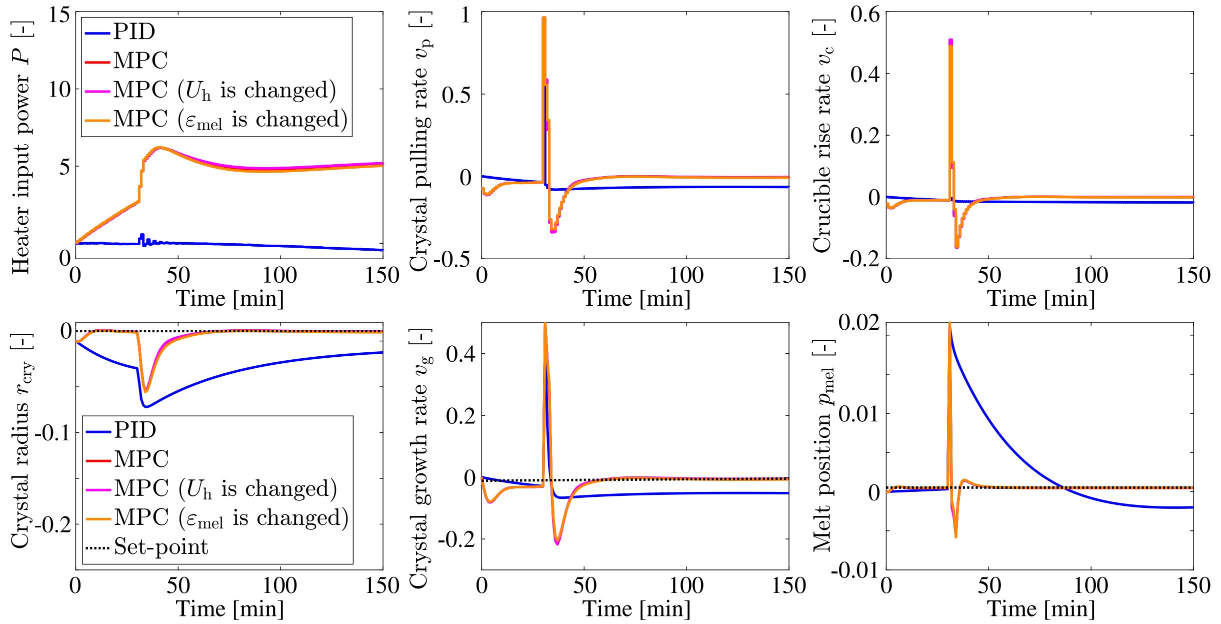

(a) Result for 150 minutes.

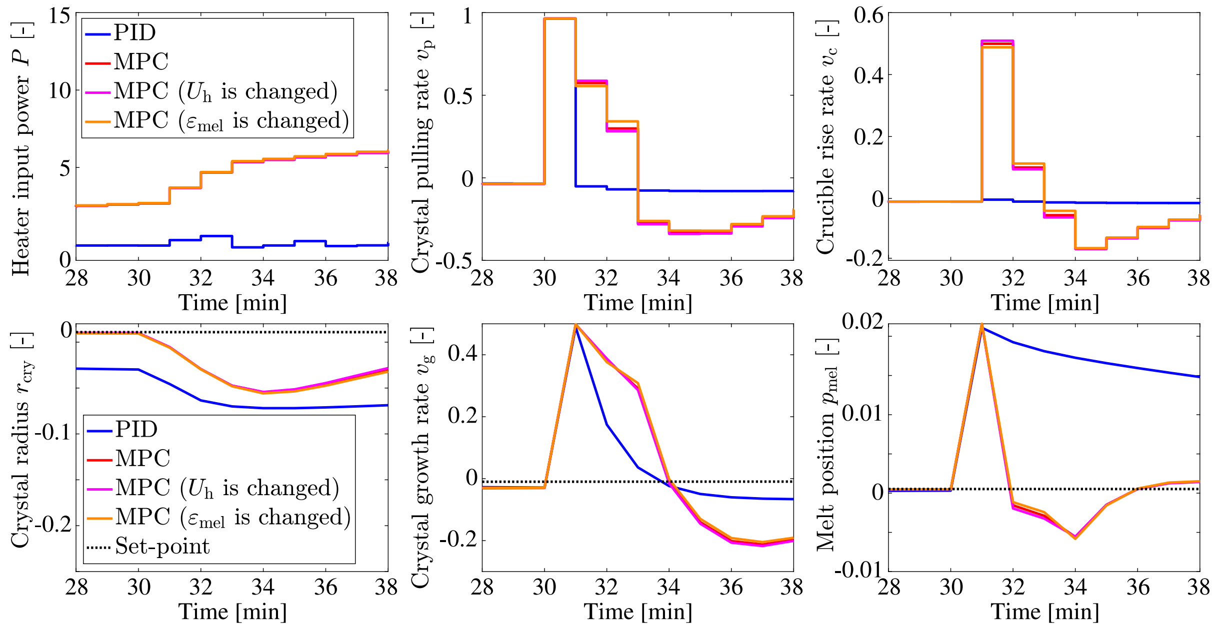

(b) Result from time = 28 to 38 min.

Fig. 3.2: Control simulation results in cases 19–21. The disturbance of the crystal pulling rate v_p was injected from time = 30 to 31 min.

Chapter 4

Successive model update

4.1 Introduction

To manufacture higher-quality silicon ingots, several model-based control methods have been proposed. The methods for producing silicon ingots with a large diameter (≥200 mm) are summarized in Table 4.1. Liu et al. [30] designed a control structure in which r_{cry} and T_{h} are controlled by manipulating P with constant v_{p}. Wan et al. [31] proposed a soft-sensor estimating v_{g}/G, a ratio of v_{g} to the axial temperature gradient at the solid-liquid interface. They also designed a dual closed-loop control strategy to

Table 4.1: Research on model-based control of the CZ process producing ingots with a diameter of more than 200 mm.

Reference	Controlled variable	Manipulated variable	Crystal diameter [mm]
Liu et al. [30]	r_{cry}, T_{h}	P	208
Wan et al. [31]	r_{cry}, v_{g}/G	P	209
Ren et al. [23]	r_{cry}, T_{h}	P, v_{p}	208
Ren et al. [24]	r_{cry}	P, v_{p}	209
Zhang et al. [18]	r_{cry}, T_{h}	P, v_{p}	300
Lee et al. [17]	r_{cry}, T_{h}	P, v_{p}	200, 300
Chapter 3	r_{cry}, v_{g}, p_{mel}	P, v_{p}, v_{c}	300

control r_{cry} and v_{g}/G. Ren et al. [23] constructed a deep neural network by combining a stacked autoencoder (SAE) and a long short-term memory (LSTM) network to capture the features and dynamics of the crystal growth. They used the model to design two controllers, which control r_{cry} and T_{h} by manipulating v_{p} and P, respectively. Ren et al. [24] developed a Hammerstein-Wiener model based on an LSTM network for the energy transfer process and combined the model with the hydrodynamic and geometric model. They applied the model to the control of r_{cry} and verified the effectiveness. Zhang et al. [18] and Lee et al. [17] determined a feedforward trajectory of temperature in the traditional control structure based on model predictive control (MPC).

We built the GB model that can predict the three controlled variables (CVs) in the industrial CZ process with high accuracy and proposed a nonlinear MPC method based on the GB model as shown in Chapter 3. The method improved disturbance rejection performance than the conventional industrial control method even when a plant-model mismatch exists.

In general, the control performance of model-based control relies heavily on the prediction accuracy of the CVs, and the prediction model often contains a plant-model mismatch. In Chapter 3, we used the prediction model whose parameter is different from that of the controlled process by 5% or 10%. However, in real applications, two or more parameters may differ from those of the controlled process. In addition, the parameter may differ by more than 10%. This chapter deals with the cases where one parameter of the prediction model differs from that of the controlled process by more than 10% and two parameters of the prediction model differ from those of the controlled process.

Various state estimation methods have been proposed, such as Kalman filter [50], particle filter [51], and moving horizon estimation (MHE) [52, 53]. The CZ process is characterized by a long time constant, and the present process variables are affected by the past state; thus, this study adopts MHE, which modifies the model parameters

to reproduce the time series data from the past to the present. In applying MHE, we need to select the parameters to be modified online. We use the two physical properties described in the previous chapter, U_{h} and $\varepsilon_{\mathrm{mel}}$, as the parameters to be modified. It is also difficult to derive the parameters that minimize the prediction errors of the gray-box model by solving the optimization problem. Therefore, we construct models corresponding to several candidate parameters in advance, as in grid search, and compare their prediction accuracy to obtain the suitable parameters.

Our contributions are summarised as follows:

- To develop an MPC method for updating the prediction model to compensate for the plant-model mismatch.
- To improve disturbance rejection performance of the gray-box model-based predictive control method proposed in Chapter 3.

4.2 Proposed method

This section presents a method for updating the prediction model to cope with a plant-model mismatch. The proposed method is based on moving horizon estimation (MHE), a simple state estimation method that modifies states to reproduce the past actual data. MHE is available for parameter estimation by regarding unknown parameters as unknown constant states [53]. The present study assumes that the parameters to be updated are known in advance.

In the proposed method, first, the parameters to be updated $\boldsymbol{\theta}$ and their candidates $\{\boldsymbol{\theta}_1, \cdots, \boldsymbol{\theta}_{N_{\mathrm{all}}}\}$ are determined. Then, N_{all} models are built.

After control starts, the prediction model is first updated at time $t = t_{\mathrm{u}}$, and then updated every T_{u} time steps by the following steps:

1. Select N_{s} models from N_{all} prepared models.

2. Predict the CVs from $t = t_0 - T_\mathrm{p}$ to $t = t_0$ by the N_s selected models. Actual data of MVs are input to the models.
3. Derive the nondimensionalized estimation errors of the CVs.
4. Adopt the model whose sum of the estimation errors is the smallest as the next prediction model.

In step 1, the models similar to the current prediction model are selected. The similarity between two models can be evaluated by the relative errors between their parameters. N_s is determined based on the computer performance and T_u.

In this study, two parameters in the GB model are determined to be updated: the overall heat transfer coefficient of the heater U_h and melt emissivity ε_mel. The candidates of their values are as follows:

$$U_\mathrm{h} \in \left\{440, 490, 540 \text{ W/(m}^2\text{ K)}\right\}, \tag{4.1}$$

$$\varepsilon_\mathrm{mel} \in \{0.21, 0.23, 0.25, 0.27, 0.29\}. \tag{4.2}$$

U_h cannot be measured and its true value is unknown; we used 440 W/(m^2 K), 490 W/(m^2 K), and 540 W/(m^2 K). The candidates of ε_mel were determined based on the fact that the experimental values [47] and the values used in past studies [32, 34, 48] are between 0.2 and 0.3, and that the CVs predicted by the GB model change significantly when ε_mel changes by about 0.02.

In the offline preparation, we built fifteen GB models ($N_\mathrm{all} = 15$) for all combinations of candidates of U_h and ε_mel in Eqs. (4.1) and (4.2). It took about 30 minutes to build one statistical model using Quad-Core Intel Core i5 CPU (2.3GHz). In online procedure, all of the models are selected in step 1: $N_\mathrm{s} = 15$.

4.3 Simulation condition

We evaluated the disturbance rejection performance of the conventional method without a model update and the proposed method with a model update, labeled C_1–C_3 and P_1–P_{12} respectively, as shown in Table 4.2. We used GB model 1 in which U_h = 490 W/(m^2 K) and $\varepsilon_{mel} = 0.25$ as the controlled process. To investigate the effect of a plant-model mismatch to the control performance, in C_1–C_3, we used three GB models: GB model 1, GB model 2 (U_h = 490 W/(m^2 K), $\varepsilon_{mel} = 0.21$) and GB model 3 (U_h = 540 W/(m^2 K), $\varepsilon_{mel} = 0.27$). In P_1–P_{12}, GB models 2 and 3 were used as the initial prediction model. To investigate the effect of the parameters T_u and T_p, we used six different combinations. For each simulation, the sampling interval, the control interval Δt_c, and the linearization interval Δt_l were 1 min. $H_p = 60$ min, $H_c = 10$ min, and weighting matrices were as follows:

$$\boldsymbol{Q} = \text{diag}\left(\frac{100}{\epsilon_{y_1,\max}}, \frac{100}{\epsilon_{y_2,\max}}, \frac{100}{\epsilon_{y_3,\max}}\right), \tag{4.3}$$

$$\boldsymbol{R} = \text{diag}\left(\frac{1}{\Delta u_{1,\max}}, \frac{1}{\Delta u_{2,\max}}, \frac{1}{\Delta u_{3,\max}}\right). \tag{4.4}$$

The control simulation was conducted in the following procedure:

1. Determine the initial condition and start control simulation.
2. Conduct the first model update after 30 minutes when using the method with a model update.
3. Inject a constant disturbance during one minute into one of the MVs or the CVs except for v_g after 60 minutes from the start. The magnitude of the disturbance to the MV and the CV is $\Delta u_{i,\max}$ and $\epsilon_{y_i,\max}$, respectively.
4. Continue the simulation for next 120 minutes.

$\epsilon_{y_i,\max}$ is the maximum absolute control error of the ith CV in one-batch industrial process data. In step 2, the model updates started after 30 min so that the update simultaneously occurs as early as possible.

We compared the control performance at the early, middle, and late stages, considering the dynamic characteristics of the CZ process change as the crystal grows. The crystal length is 0–33%, 33–66%, and 66–100% of the product's crystal length at the early, middle, and late stages. We used five patterns of disturbances at three stages; thus, control simulations were conducted in 15 cases as shown in Table 4.2.

4.4 Results and Discussion

Figure 4.1 shows the results in cases 2, 7, and 12 in C_1, C_2, and P_4–P_6. The IAEs of the CVs nondimensionalized by $\epsilon_{y_i,\max}$ for 120 minutes after the disturbance injection are compared. The results are summarized in Table 4.2. Each sum of IAEs was divided by that in C_1, which is the value in parentheses in the table. The orders of the sums are different between cases in C_1 because the CVs changed more significantly when the disturbance was injected into the CV than when the disturbance was injected into the MV. In cases 4 and 5 in C_2 and case 14 in P_1, each IAE was calculated based on the simulation results for shorter than 120 min. This is because v_g became negative before the 120 minutes simulation, and the simulation was aborted.

As shown in Table 4.2, the sums of IAEs in C_2 are larger than those in C_1 in all cases except for case 3. The sums of IAEs in C_3 are equal to or smaller than those in C_1 in 11/15 cases, and the mean is the same as that in C_1. This is because the prediction accuracy of the CVs by GB model 2 is lower than that by GB model 1, while that by GB model 1 and that by GB model 3 are almost the same.

The reason why the prediction accuracy of GB model 3 was almost the same as GB model 1 is shown below. If U_h becomes large in the first-principle model, T_h decreases

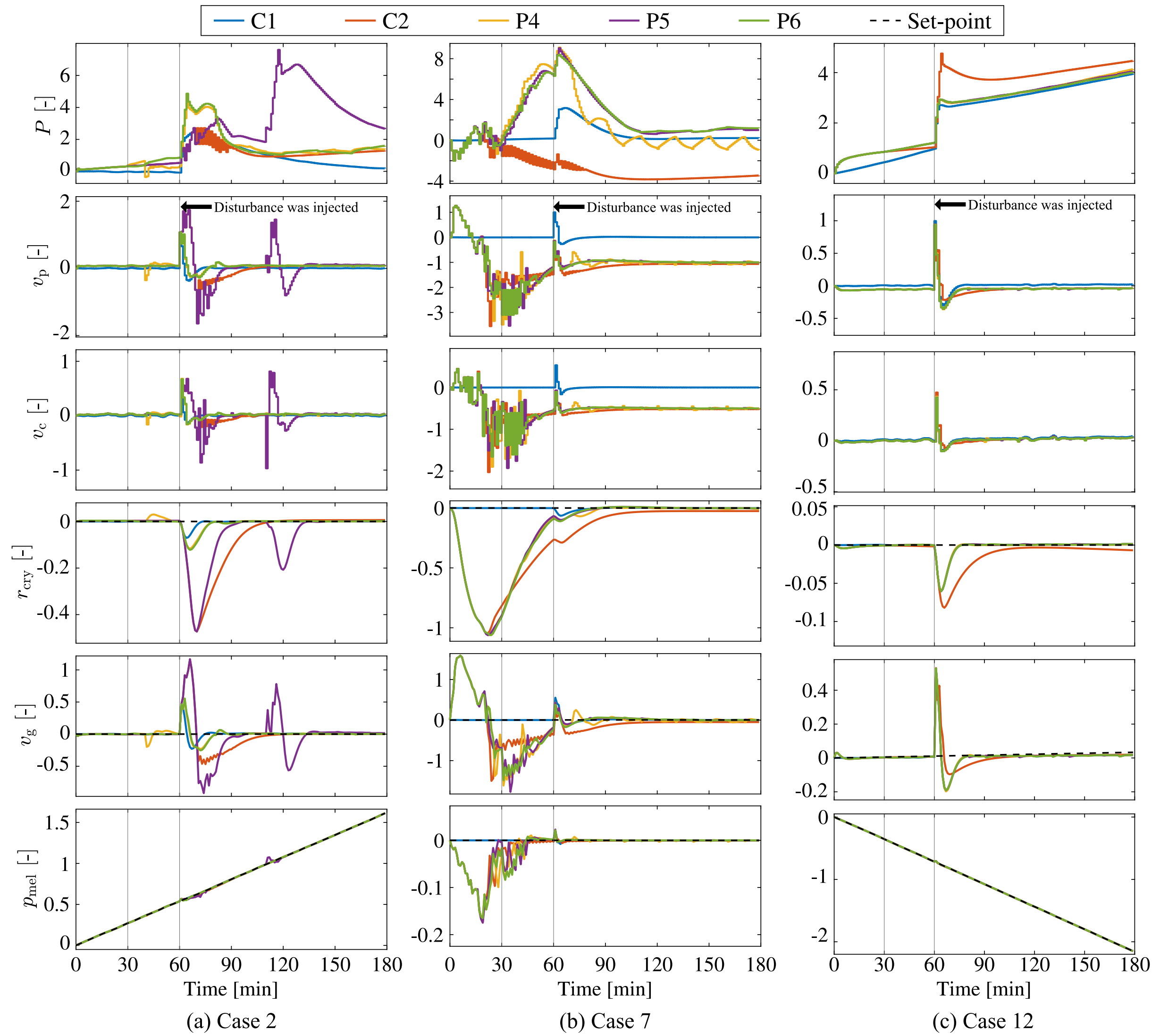

Fig. 4.1: Control simulation results in cases 2, 7 and 12 in C_1, C_2, P_4, P_5, and P_6. The model update started at Time=30 min, and the disturbance was injected into v_p at Time=60 min.

and the heat transfer rate from the heater to the melt becomes small, leading to a decrease in $\frac{dT_{mel}}{dt}$. If ε_{mel} becomes large, in the first-principle model, the radiative heat transfer rate from the melt increases, leading to a decrease in $\frac{dT_{mel}}{dt}$. If T_{mel} becomes small, G_{men} becomes large. In the statistical model in the GB model, when T_{mel} becomes small, the predicted value of G_{cry} becomes large, as represented in Chapter 2. The prediction accruacy of v_g is dependent on $k_{men}G_{men} - k_{cry}G_{cry}$, which is the numerator

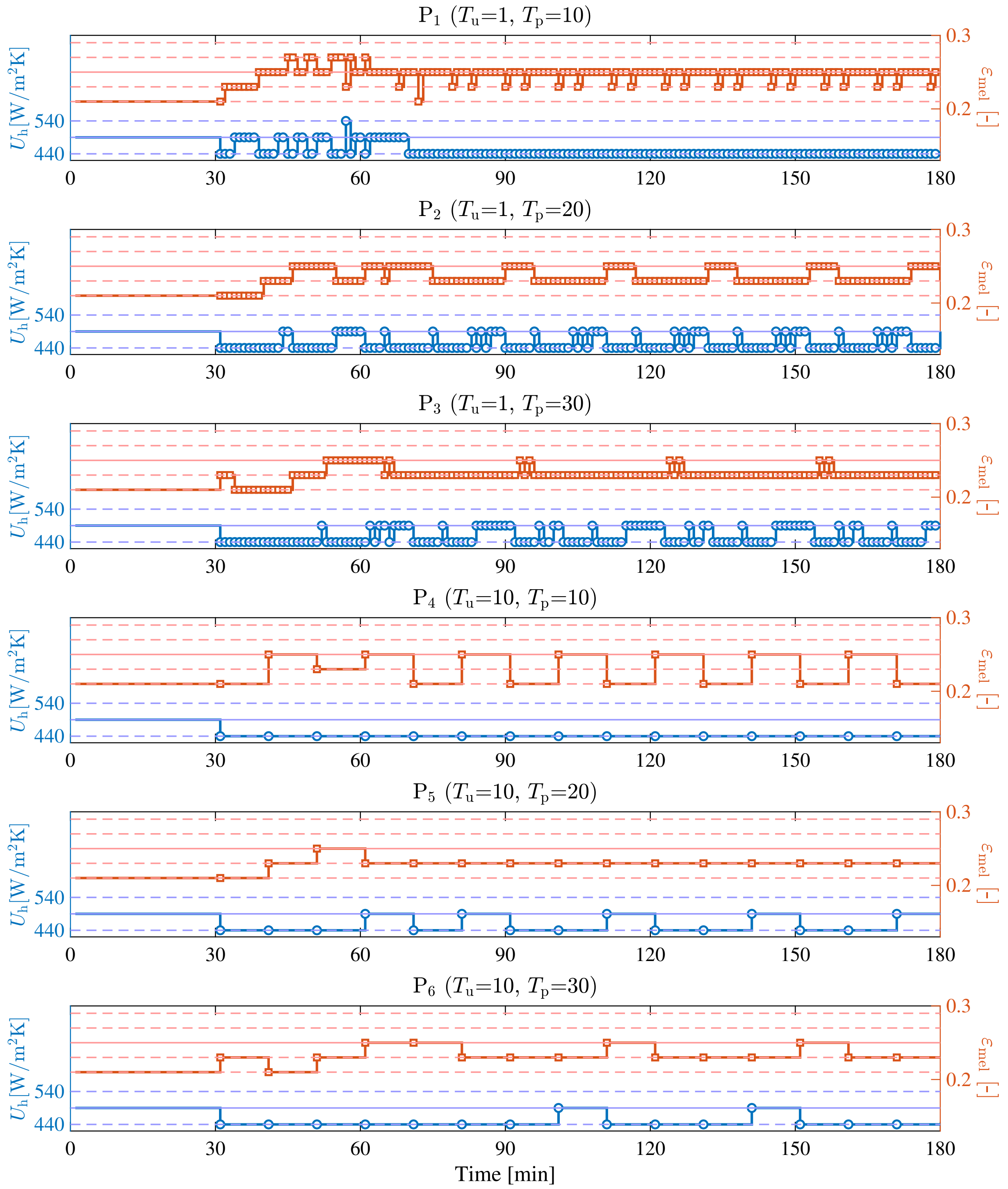

Fig. 4.2: U_h and ε_mel of the selected prediction model at each sampling interval in case 7 of P_1–P_6.

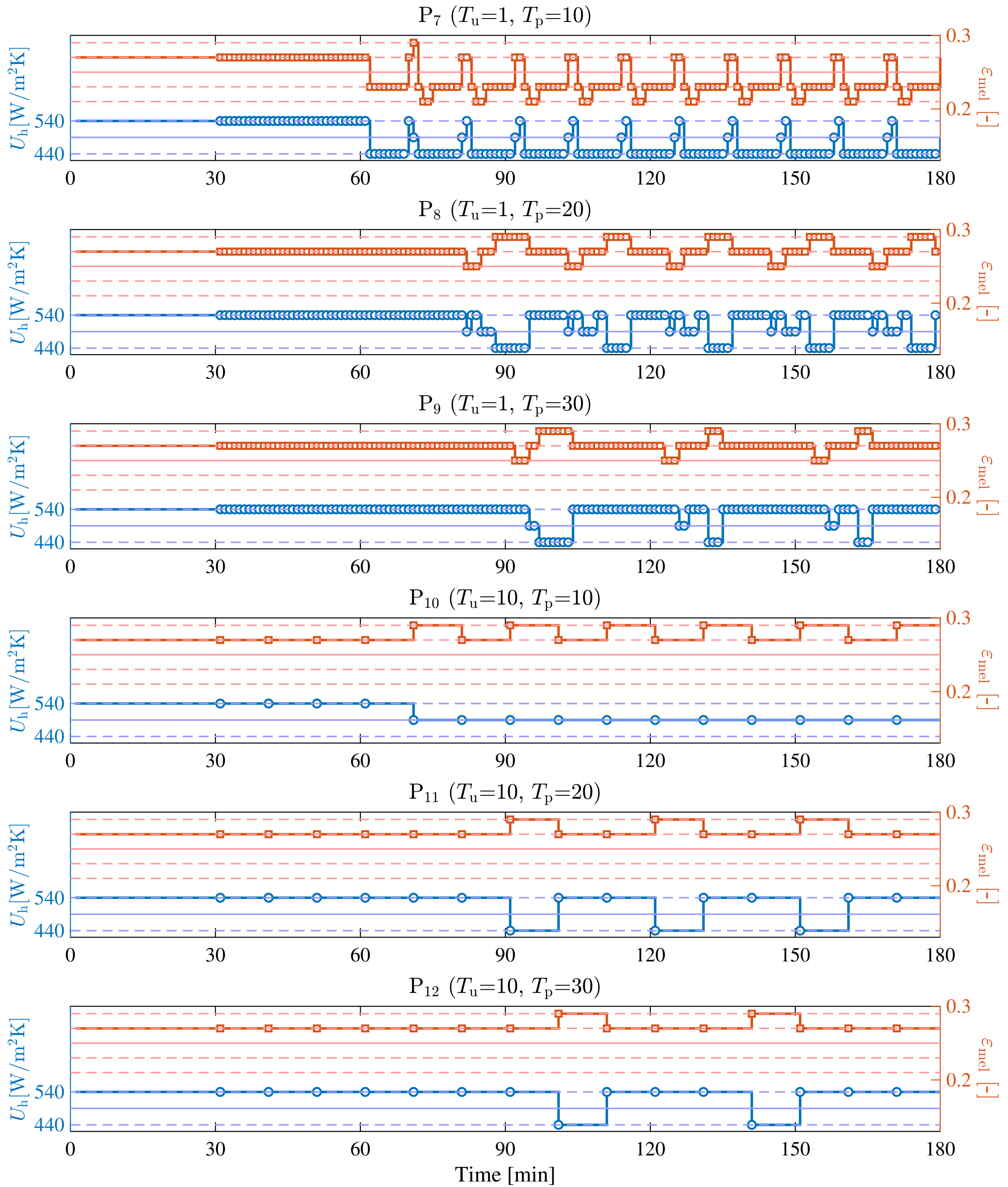

Fig. 4.3: U_{h} and $\varepsilon_{\mathrm{mel}}$ of the selected prediction model at each sampling interval in case 7 of P_7–P_{12}.

in Eq. (2.12), and affects the prediction accuracy of r_{cry} and φ. In GB model 3, the changes in $k_{\mathrm{men}}G_{\mathrm{men}}$ and $k_{\mathrm{cry}}G_{\mathrm{cry}}$ from those of GB model 1 are almost the same, and hence the prediction accuracy of the CVs and the IAEs are almost the same.

Table 4.2 shows that the mean of the sums of IAEs in P_1–P_6 are smaller than that in C_2, and that in P_8–P_{12} is the same as that in C_3. The sums of IAEs in P_1–P_6 and P_7–P_{12} are smaller than those in C_2 and C_3 in 78/90 and 50/90 simulations, respectively. Although the sums of IAEs in P_1–P_{12} are larger in the other simulations, the proposed method did not significantly deteriorate the control performance.

In Fig. 4.1, each vertical axis of the MVs and the CVs is nondimensionalized by $\Delta u_{i,\max}$ and $\epsilon_{y_i,\max}$, respectively, and shifted so that each initial value is zero. In case 2, the control errors of r_{cry} and v_{g} in P_4 and P_6 are smaller and reduced faster than those in C_2. In case 2 in P_5, the control errors of r_{cry} and v_{g} for Time=110—130 min are larger than those in C_2 because the prediction performance of the CVs by the selected model was insufficient. In case 7, the control errors of r_{cry} and v_{g} in P_4–P_6 are smaller and reduced faster than that in C_2. In case 12, the control errors of r_{cry} in P_4–P_6 are smaller and reduced faster than that in C_2, and those of v_{g} in P_4–P_6 immediately after the disturbance rejection are larger but reduced faster than those in C_2, resulting in the smaller sum of IAEs.

Figures 4.2 and 4.3 show the parameters of the selected prediction model in case 7 in P_1–P_6 and P_7–P_{12}, respectively. The marker symbols represent the timing of the model update. The horizontal lines represent candidate values of U_{h} and $\varepsilon_{\mathrm{mel}}$, and the solid blue and red lines represent their correct values. The trajectories of the parameters of the selected prediction models are different. The comparison between P_1–P_3 and P_4–P_6 and that between P_7–P_9 and P_{10}–P_{12} show that the change in T_{u} or T_{p} does not highly affect the disturbance rejection performance.

The proposed method achieved high disturbance rejection performance even when the selected U_{h} and $\varepsilon_{\mathrm{mel}}$ are different from those of GB model 1. This is because the model

with a plant-model mismatch can sometimes predict the CVs with high accuracy, such as GB model 3.

4.5 Conclusion

We proposed a method for updating the prediction model in MPC to achieve high disturbance rejection performance even when a large plant-model mismatch exists. The control performance of MPC with the proposed model update method was compared with the conventional method without a model update through control simulations. The results demonstrated that the proposed method achieved higher disturbance rejection performance than the conventional one in 128/180 simulations.

Table 4.2: Sum of IAEs of three controlled variables for each case using methods with and without model update. Each sum of IAEs was divided by that of C_1, which is the value in parentheses.

		Label	C_1	C_2	C_3	P_1	P_2	P_3	P_4	P_5	P_6
		Initial prediction model	1	2	3	2					
		Model update	No			Yes					
		T_u	—			1	1	1	10	10	10
		T_p	—			10	20	30	10	20	30
Case	Stage	Disturbance	Ratio of sum of IAEs to that in C1 (original sum of IAEs)								
1	Early	P	1.0 (0.34)	3.0	0.84	1.6	7.1	4.0	1.6	3.0	1.8
2		v_p	1.0 (3.8)	6.9	0.91	1.3	0.89	0.93	1.6	9.1	1.7
3		v_c	1.0 (2.9)	1.0	0.60	1.2	0.94	0.95	1.1	0.86	1.2
4		r_{cry}	1.0 (32)	21 *	1.1	1.2	1.5	1.1	1.3	2.5	1.5
5		p_{mel}	1.0 (15)	42 *	0.89	1.2	1.2	2.0	4.0	8.9	4.0
6	Middle	P	1.0 (0.30)	61	1.1	11	12	12	12	9.7	12
7		v_p	1.0 (3.8)	5.6	1.0	1.3	1.5	1.4	2.1	1.4	1.5
8		v_c	1.0 (2.8)	8.1	1.0	1.6	1.8	1.5	1.9	1.6	1.8
9		r_{cry}	1.0 (32)	1.8	1.1	1.6	14	2.9	1.2	1.5	2.0
10		p_{mel}	1.0 (25)	1.4	1.0	1.1	1.1	1.3	1.0	1.2	1.0
11	Late	P	1.0 (1.9)	1.2	1.0	0.95	0.95	1.0	0.95	1.0	1.0
12		v_p	1.0 (4.6)	1.4	1.0	1.2	1.0	1.0	1.0	1.0	1.0
13		v_c	1.0 (4.1)	1.1	1.0	1.3	1.0	1.3	1.0	1.0	1.0
14		r_{cry}	1.0 (30)	26	1.1	1.0	3.4	1.1	1.1	1.1	1.3
15		p_{mel}	1.0 (16)	62	0.87	1.0 *	1.4	1.0	0.94	1.0	1.0
	Mean		1.0 (12)	16	1.0	1.9	3.3	2.2	2.2	3.0	2.3

		Label	P_7	P_8	P_9	P_{10}	P_{11}	P_{12}
		Initial prediction model	3					
		Model update	Yes					
		T_u	1	1	1	10	10	10
		T_p	10	20	30	10	20	30
Case	Stage	Disturbance	Ratio of sum of IAEs to that in C1					
1	Early	P	0.84	1.0	1.1	0.84	0.84	1.0
2		v_p	1.0	1.0	1.0	0.91	0.91	0.93
3		v_c	0.64	0.6	0.63	0.60	0.59	0.61
4		r_{cry}	1.6	1.0	1.1	1.3	1.2	1.2
5		p_{mel}	1.0	1.0	1.0	0.88	0.88	0.88
6	Middle	P	1.1	1.1	1.1	1.1	1.1	1.1
7		v_p	1.6	1.1	1.1	1.1	1.1	1.1
8		v_c	1.4	1.2	1.1	1.1	1.1	1.1
9		r_{cry}	1.1	1.2	1.6	1.2	1.1	1.4
10		p_{mel}	1.1	1.2	0.92	0.82	0.80	0.82
11	Late	P	1.0	1.0	1.0	1.0	1.0	1.0
12		v_p	1.2	1.0	1.0	1.0	1.0	1.0
13		v_c	1.0	1.0	1.0	1.0	1.0	1.0
14		r_{cry}	1.0	1.1	1.1	1.1	1.1	1.1
15		p_{mel}	0.92	0.94	0.92	0.87	0.87	0.88
	Mean		1.1	1.0	1.0	1.0	1.0	1.0

* The IAEs were calculated using the simulation result for shorter than 120 minutes.

Chapter 5

Conclusion / Future Perspectives

5.1 Summary

In this dissertation, a gray-box model was developed for the CZ process, which manufactures single-crystal silicon ingots with a diameter of 300 mm, and a control system based on the model was developed.

In Chapter 1, we explained the recent market of the semiconductor industry and the necessity of improving the control performance of the CZ process, which is mainly used for producing monocrystalline silicon ingots. Then, the current control structure used in the industrial CZ process was shown, and the previous studies on control systems of the CZ process were summarized to clarify the purpose of the present thesis. A control method based on the first-principle model is effective to achieve higher control performance considering the nonlinearity and the time-varying input-output relationship of the CZ process. In this study, a gray-box model was constructed by improving the first-principle model constructed by Zheng et al. [32].

In Chapter 2, the method of building the gray-box model and the prediction results were presented. We first described the issues of the first-principle model and then proposed a method to estimate the variable that affects the prediction accuracy of the

control variables using a statistical model. In addition, we showed how to determine the values of unmeasurable variables necessary for building the statistical model. We estimated the state of the process at the start of prediction using the same method, and the prediction enables us to predict the controlled variables at any point. The prediction accuracy of the proposed gray-box model was higher than the first-principle model for multiple ingot production data.

In Chapter 3, we proposed a model predictive control method based on the gray-box model. The gray-box model consists of complex differential-algebraic equations, and a high computational load is required to solve the optimization problem using the gray-box model in the model predictive control framework. To reduce the computational load, we proposed a method for deriving a prediction model by successive linearization of the gray-box model. The behavior of the linear model changed among the three different stages of the crystal pulling process, and it was confirmed that successive linearization is necessary to represent the time-varying input-output relationship of the gray-box model. This chapter compared the proposed control method with the control method used in the industrial CZ processes through control simulations. The proposed method improved the disturbance rejection performance, and the control performance of the proposed method was better than that of the conventional method even when one of the parameters in the prediction model was different from that of the controlled process by 10%.

In Chapter 4, in order to utilize the gray-box model-based predictive control method over a long period, a method for dealing with a plant-model mismatch derived from the estimation error of the physical properties in the actual process is investigated. In order to reduce the effect of the mismatch, it is practical to update the prediction model so that the next prediction model achieves higher prediction accuracy. In this chapter, under the assumption that the variables owing to a plant-model mismatch are known, a method to avoid degradation of control performance due to the mismatch is

examined. The gray-box model is complex and requires a high computational load when the controlled variables need to be predicted many times. In addition, it is challenging to clarify the relationship between the prediction accuracy of the gray-box model and the variables. Therefore, we proposed a method for preparing several gray-box models in advance and updating the prediction model online by comparing their estimation accuracy. We compared the control performance of gray-box model-based predictive control methods with and without a modeling error through several simulations where the plant-model mismatch is more significant than that in Chapter 3, and showed that the method with model update improves the performance.

Through the investigations in Chapters 2 to 4, we 1) developed a gray-box model that predicts three controlled variables with high accuracy for operation data of multiple ingots, which was not possible with the existing methods; 2) developed a nonlinear model predictive control method using successive linearization of the gray-box model; and 3) proposed a model update method to deal with a plant-model mismatch in which multiple parameters in the prediction model and the controlled process are different.

5.2 Future Outlooks

The next step is to apply the developed method to the actual process. First, it is necessary to verify whether the parameters in the gray-box model are adequate or not. This is because in this dissertation, two parameters (the overall heat transfer coefficient of the heater U_{h} and melt emissivity $\varepsilon_{\mathrm{mel}}$) of the prediction model are different from those of the controlled process. However, this investigation may not be sufficient to prove the effects of the parameters in the model on the prediction performance. The prediction accuracy should be validated using several operation data to confirm that the gray-box model has satisfactory prediction accuracy. Following the above validation, experiments in the actual furnace will be conducted to confirm that the proposed method

can produce higher-quality ingots than the conventional control method. Finally, the method will be applied to the commercial process.

On the other hand, there remain some problems with the method.

1. The proposed method works well in the body growth section. However, it cannot be used when the crystal changes significantly, especially in crowning and tailing parts, because the proposed method estimates the state at the beginning of the prediction based on the quasi-steady-state assumption. To achieve high control performance even when the crystal changes, a method to estimate the state of the process at the beginning of the prediction is required.
2. This dissertation assumed that all variables could be measured without noise. In the CZ process, it is difficult to measure the process variables accurately. For example, the radius of the Si ingot is usually estimated based on the bright ring taken by the camera above the melt [22]. The radius measured from the bright ring is different from the actual one and affects the control performance of the crystal radius [54–57]. In addition, the measured values of the variables contain noise, so it is necessary to remove the noise appropriately. The methods for measuring the variables with high accuracy have been studied [58].

By solving these issues and combining them with the control method proposed in this dissertation, we will be able to achieve higher control performance in real processes.

References

1) Silicon shipment statistics — semi, https://www.semi.org/en/products-services/market-data/materials/si-shipment-statistics, (Accessed on 09/29/2021).

2) Silicon wafer shipments reach new high in second quarter 2021, semi reports — semi, https://www.semi.org/en/news-media-press/semi-press-releases/silicon-wafer-shipments-reach-new-high-second-quarter-2021-semi-reports, (Accessed on 09/29/2021).

3) Wsts_nr-2021_06.pdf, https://www.wsts.org/esraCMS/extension/media/f/WST/5088/WSTS_nr-2021_06.pdf, (Accessed on 09/29/2021).

4) V. Prakash, A. Agarwal, and E.K. Mussada. Processing Methods of Silicon to its Ingot: a Review. *Silicon*, **11**(3), 1617–1634, 2019.

5) L. Wu. *Modeling and simulation of Czochralski bulk crystal growth process: investigation of transport effects in melt and gas phases.* 2009.

6) W. von Ammon. FZ and CZ crystal growth: Cost driving factors and new perspectives. *Phys. Status Solidi A*, **211**(11), 2461–2470, 2014.

7) P.V. Zant. *Microchip Fabrication, Sixth Edition.* McGraw-Hill Education, New York, 6th ed. edition, 2014.

8) J. Evers, P. Klüfers, R. Staudigl, and P. Stallhofer. Czochralski's creative mistake: a milestone on the way to the gigabit era. *Angew. Chem. Int. Ed Engl.*, **42**(46), 5684–5698, 2003.

9) A.P. Mozer. New developments in silicon czochralski crystal growth and wafer technology. *Mater. Sci. Eng. B*, **73**(1), 36–41, 2000.

10) M. Hourai, T. Nagashima, H. Nishikawa, W. Sugimura, T. Ono, and S. Umeno. Review and comments for the development of point defect-controlled CZ-Si crystals and their application to future power devices. *Phys. Status Solidi A*, **216**(10), 1970035, 2019.

11) M.A. Gevelber, M.J. Wargo, and G. Stephanopoulos. Advanced control design considerations for the czochralski process. *J. Cryst. Growth*, **85**(1-2), 256–263, 1987.

12) M.A. Gevelber, G. Stephanopoulos, and M.J. Wargo. Dynamics and control of the czochralski process II. objectives and control structure design. *J. Cryst. Growth*, **91**, 199–217, 1988.

13) M.A. Gevelber. Dynamics and control of the czochralski process III. interface dynamics and control requirements. *J. Cryst. Growth*, **139**, 271–285, 1994.

14) M.A. Gevelber. Dynamics and control of the czochralski process IV. control structure design for interface shape control and performance evaluation. *J. Cryst. Growth*, **139**, 286–301, 1994.

15) J. Winkler, M. Neubert, and J. Rudolph. Nonlinear model-based control of the Czochralski process I: Motivation, modeling and feedback controller design. *J. Cryst. Growth*, **312**, 1005–1018, 2010.

16) J. Winkler, M. Neubert, and J. Rudolph. Nonlinear model-based control of the

czochralski process II: Reconstruction of crystal radius and growth rate from the weighing signal. *J. Cryst. Growth*, **312**, 1019–1028, 2010.

17) K. Lee, D. Lee, J. Park, and M. Lee. MPC based feedforward trajectory for pulling speed tracking control in the commercial Czochralski crystallization process. *Int. J. Control Autom. Syst.*, **3**(2), 252–257, 2005.

18) J. Zhang, D. Liu, and Y. Zhao. GPC based adaptive crowning growth control in CZ-Si process. In *2016 35th Chinese Control Conference (CCC)*, 211–215, 2016.

19) J. Ng and S. Dubljevic. Optimal control of convection-diffusion process with time-varying spatial domain: Czochralski crystal growth. In *J. Process Control*, **21**, 1361–1369, 2011.

20) J. Ng, I. Aksikas, and S. Dubljevic. Control of parabolic PDEs with time-varying spatial domain: Czochralski crystal growth process. *Int. J. Control*, **86**(9), 1467–1478, 2013.

21) P.K.C. Wang. Feedback control of a heat diffusion system with time - dependent spatial domain. *Optim. Control Appl. Methods*, **16**(5), 305–320, 1995.

22) J. Winkler, M. Neubert, and J. Rudolph. A review of the automation of the Czochralski crystal growth process. *Acta Phys. Pol. A*, **124**(2), 181–192, 2013.

23) J.C. Ren, D. Liu, and Y. Wan. Model-Free adaptive iterative learning control method for the czochralski silicon monocrystalline batch process. *IEEE Trans. Semicond. Manuf.*, **34**(3), 398–407, 2021.

24) J.C. Ren, D. Liu, and Y. Wan. Modeling and application of czochralski silicon single crystal growth process using hybrid model of data-driven and mechanism-based methodologies. *J. Process Control*, **104**, 74–85, 2021.

25) R. Irizarry-Rivera and W.D. Seider. Model-predictive control of the Czochralski crystallization process. Part I. Conduction-dominated melt. *J. Cryst. Growth*, **178** (4), 593–611, 1997.

26) R. Irizarry-Rivera and W.D. Seider. Model-predictive control of the Czochralski crystallization process. Part II. Reduced-order convection model. *J. Cryst. Growth*, **178**(4), 612–633, 1997.

27) J. Abdollahi, M. Izadi, and S. Dubljevic. Model predictive temperature tracking in crystal growth processes. *Comput. Chem. Eng.*, **71**, 323–330, 2014.

28) P. Rahmanpour, S. Sælid, M. Hovd, O. Grønning, and M. Jomaa. Nonlinear model predictive control of the Czochralski process. *IFAC-PapersOnLine*, **49**(20), 120–125, 2016.

29) P. Rahmanpour, S. Sælid, and M. Hovd. Run-To-Run control of the czochralski process. *Comput. Chem. Eng.*, **104**, 353–365, 2017.

30) D. Liu, N. Zhang, L. Jiang, X. Zhao, and W. Duan. Nonlinear generalized predictive control of the crystal diameter in CZ-Si crystal growth process based on stacked sparse autoencoder. *IEEE Trans. Control Syst. Technol.*, **28**(3), 1132–1139, 2020.

31) Y. Wan, D. Liu, C.C. Liu, and J.C. Ren. Data-driven model predictive control of cz silicon single crystal growth process with v/g value soft measurement model. *IEEE Trans. Semicond. Manuf.*, **34**(3), 420–428, 2021.

32) Z. Zheng, T. Seto, S. Kim, M. Kano, T. Fujiwara, M. Mizuta, and S. Hasebe. A first-principle model of 300 mm Czochralski single-crystal Si production process for prediction crystal radius and crystal growth rate. *J. Cryst. Growth*, **492**, 105–113, 2018.

33) D. Megías, J. Serrano, and M.Y.E. Ghoumari. Extended linearised predictive con-

trol: Practical control algorithms for non-linear systems. In *1999 European Control Conference (ECC)*, 2707–2712, 1999.

34) M.A. Gevelber and G. Stephanopoulos. Dynamics and control of the Czochralski process. I. Modelling and dynamic characterization. *J. Cryst. Growth*, **84**, 647–668, 1987.

35) M. Neubert and J. Winkler. Nonlinear model-based control of the Czochralski process III: Proper choice of manipulated variables and controller parameter scheduling. *J. Cryst. Growth*, **360**, 3–11, 2012.

36) G. Satunkin. Modelling the dynamics and control design for czochralski, liquid encapsulated czochralski and floating zone processes. *Prog. Cryst. Growth Charact. Mater.*, **56**(1-2), 1–121, 2010.

37) J. Abdollahi and S. Dubljevic. Crystal radius and temperature regulation in Czochralski crystallization process. In *Proceedings of the American Control Conference*, 1626–1632, 2013.

38) J. Abdollahi, M. Izadi, and S. Dubljevic. Temperature distribution reconstruction in czochralski crystal growth process. *AIChE Journal*, **60**(8), 2839–2852, 2014.

39) I. Ahmad, A. Ayub, M. Kano, and I.I. Cheema. Gray-box soft sensors in process industry: Current practice, and future prospects in era of big data. *Processes*, **8** (2), 243, 2020.

40) I. Ahmad, M. Kano, S. Hasebe, H. Kitada, and N. Murata. Gray-box modeling for prediction and control of molten steel temperature in tundish. *J. Process Control*, **24**, 375–382, 2014.

41) J.J. Derby and R.A. Brown. On the quasi-steady-state assumption in modeling czochralski crystal growth. *J. Cryst. Growth*, **87**(2), 251–260, 1988.

42) C.E. Rasmussen and C.K. Williams. *Gaussian processes for machine learning*, **2**. The MIT Press, Cambridge, MA, 2006.

43) A. Ferguson. LXXXIX. On the shape of the capillary surface formed by the external contact of a liquid with a cylinder of large radius. *Philos. Magaz.*, **24**(144), 837–844, 1912.

44) Cgsim — str software for modeling of crystal growth, epitaxy, and semiconductor devices, `https://www.str-soft.com/software/cgsim/`, (Accessed on 10/03/2021).

45) J.J. Derby, L.J. Atherton, P.D. Thomas, and R.A. Brown. Finite-element methods for analysis of the dynamics and control of Czochralski crystal growth. *J. Sci. Comput.*, **2**(4), 297–343, 1987.

46) M. Jimoh and A. Dan'Isa. State space model realization using step response data of MIMO system with input delays for model predictive control. *Acta Period. Technol.*, (50), 93–104, 2019.

47) E. Takasuka, E. Tokizaki, K. Terashima, and S. Kimura. Emissivity of liquid silicon in visible and infrared regions. *J. Appl. Phys.*, **81**(9), 6384–6389, 1997.

48) A. Kondratyev, S. Demina, A. Smirnov, V. Kalaev, G. Ratnieks, L. Kadinski, and A. Sattler. 3D unsteady and steady modeling of heat and mass transfer during cz si crystal growth with a horizontal magnetic field. *Int. J. Heat Mass Transf.*, **178**, 121604, 2021.

49) S. Skogestad and C. Grimholt. *The SIMC method for smooth PID controller tuning*, 147–175. Springer, London, 2011.

50) R.E. Kalman. A new approach to linear filtering and prediction problems. *J. Basic Eng.*, **82**(1), 35–45, 1960.

51) J.B. Rawlings and B.R. Bakshi. Particle filtering and moving horizon estimation. *Comput. Chem. Eng.*, **30**(10-12), 1529–1541, 2006.

52) H. Michalska and D.Q. Mayne. Moving horizon observers and observer-based control. *IEEE Trans. Automat. Contr.*, **40**(6), 995–1006, 1995.

53) T. Ohtsuka. Nonlinear Receding-Horizon state estimation with unknown disturbances. *Trans. of the Society of Instrument and Control Engineers*, **35**(10), 1253–1260, 1999.

54) P. Rahmanpour, M. Hovd, and J.A. Bones. Nonlinear state estimation in the czochralski process. In *IFAC Proceedings Volumes*, **47**, 4891–4896, 2014.

55) H.Z. Bukhari, M. Hovd, and J. Winkler. Limitations on control performance in the czochralski crystal growth process using bright ring measurement as a controlled variable. In *IFAC-PapersOnLine*, **52**, 129–134, 2019.

56) H.Z. Bukhari, M. Hovd, and J. Winkler. Inverse response behaviour in the bright ring radius measurement of the czochralski process II: Mitigation by control. *J. Cryst. Growth*, **568-569**, 126013, 2021.

57) H.Z. Bukhari, M. Hovd, and J. Winkler. Inverse response behaviour in the bright ring radius measurement of the czochralski process I: Investigation. *J. Cryst. Growth*, **568-569**, 126039, 2021.

58) X. Zhang, D. Liu, H. Jiang, and J. Liang. Particle filter with unknown statistics to estimate liquid level in the silicon Single-Crystal growth. *IEEE Trans. Instrum. Meas.*, **69**(6), 2759–2770, 2020.

Acknowledgements

I express my deepest gratitude to my supervisor Professor Manabu Kano. I am profoundly thankful to him for his keen guidance throughout the writing of my thesis and journal, as well as his kind support and an unimpeded research environment. I sincerely appreciate the strong support extended to me by my co-supervisor, Associate Professor Sanghong Kim, at Tokyo University of Agriculture and Technology. He developed the first-principle model on which this research is based and guided me since I was a master's student. I am also grateful for the strong support of my supervisor during my master's program, Professor Shinji Hasebe, at Kyoto University. In addition to his fervent support and guidance, he also gave me advice not only on my research, but also on my career path, which helped me to make the decision to go on to a doctoral course. I express my gratitude to Mr. Toshiyuki Fujiwara and Mr. Masahiko Mizuta at SUMCO Corporation for their support in answering my questions about the CZ process in the whole course of this research. I also express my gratitude to SUMCO Corporation for providing me with data to carry out this research.

In my first-year doctoral course, I was a recipient of The Iwadare Scholarship Foundation. Thanks to the scholarship, I was able to devote myself to research.

I express my heartfelt gratitude to the members of the human systems laboratory and secretaries who advised and supported me. I would also like to thank the members of the process systems laboratory in Kyoto University. Finally, I would like to express my gratitude to my family, who has supported me throughout my life.

Publications

1. S. Kato, S. Kim, M. Kano, T. Fujiwara, and M. Mizuta, Gray-box modeling of 300 mm diameter Czochralski single-crystal Si production process, *J. Cryst. Growth*, **553**, 125929, 2021. (Correspond to Chapter 2)
   DOI: https://doi.org/10.1016/j.jcrysgro.2020.125929

2. S. Kato, S. Kim, M. Mizuta, M. Oshima, and M. Kano, Gray-box model-based predictive control of Czochralski process, *J. Cryst. Growth*, **573**, 126299, 2021. (Correspond to Chapter 3)
   DOI: https://doi.org/10.1016/j.jcrysgro.2021.126299

3. S. Kato, S. Kim, M. Mizuta, and M. Kano, Gray-box model-based predictive control of Czochralski process with successive model update, *J. Chem. Eng. Japan*, **55**, 154–161, 2022. (Correspond to Chapter 4)
   DOI: https://doi.org/10.1252/jcej.21we096

Conference Presentations

International conferences

1. S. Kato, S. Kim, M. Kano, T. Fujiwara, M. Mizuta, S. Hasebe, Method of estimating temperatures of heater and melt to improve prediction accuracy of gray-box model of 300 mm Czochralski single-crystal Si production process, *18th Asian Pacific Confederation of Chemical Engineering Congress (APCChE 2019), N201, Sapporo, Japan*, Sep. 23–27, 2019.

2. S. Kato, S. Kim, M. Kano, T. Fujiwara, M. Mizuta, S. Hasebe, Gray-box model for predicting crystal radius and crystal growth rate of 300 mm Czochralski single-

crystal silicon ingot production process, *AIChE Annual Meeting, 371y, Florida, US*, Nov. 10–15, 2019.

Domestic conferences

1. 加藤 祥太, 金 尚弘, 加納 学, 藤原 俊幸, 水田 匡彦, 長谷部 伸治,「Czochralski プロセスの結晶成長速度と結晶半径を予測するグレーボックスモデルの構築」, 第 63 回システム制御情報学会研究発表講演会 (SCI'19), GSa01-5, 大阪, 2019 年 5 月.

2. 入谷 賢佑, 加藤 祥太, 金 尚弘, 藤原 俊幸, 水田 匡彦, 加納 学, 外輪健一郎,「直接法を用いた Czochralski プロセスの同定」, 第 62 回自動制御連合講演会, 1L2-04, 北海道, 2019 年 11 月.

3. 加藤 祥太, 金 尚弘, 加納 学, 藤原 俊幸, 水田 匡彦,「300 mm シリコン単結晶を製造する Czochralski プロセスの結晶品質とヒーター温度の予測」, 第 7 回制御部門マルチシンポジウム (MSCS2020), 3C2-1, 徳島, 2020 年 3 月.

4. 加藤 祥太, 金 尚弘, 加納学,「逐次線形化に基づく Czochralski プロセスのグレーボックスモデル予測制御」, 第 8 回制御部門マルチシンポジウム (MSCS2021), 1F1-1, オンライン, 2021 年 3 月.

5. 加藤 祥太, 金 尚弘, 加納 学,「統計モデルに基づく状態推定を用いた Czochralski プロセスのグレーボックスモデル予測制御」, 第 65 回システム制御情報学会研究発表講演会 (SCI'21), TS03-03-3, オンライン, 2021 年 5 月.